Bulletin of Earthquake Engineering (2026) 24:93–134
https://doi.org/10.1007/s10518-025-02165-2

ORIGINAL ARTICLE

A new layered shell model for reinforced concrete walls II: experimental validation against quasi-static tests

Cem Tura[1] · Kutay Orakcal[1] · M. Fethi Gullu[2] · Alper Ilki[3]

Received: 28 June 2024 / Accepted: 28 March 2025 / Published online: 11 April 2025
© The Author(s) 2025

Abstract

Nonlinear analysis procedures used in performance-based design/assessment of structural systems with reinforced concrete walls are subject to much improvement, upon implementation of a reliable modeling approach that is capable of accurately simulating the nonlinear response characteristics of both planar and non-planar walls at both global (force-displacement, moment-rotation, torque-twist) and local (e.g., strains, shear deformations, flexural deformations) response levels under combined and multi-directional loading conditions. Towards this objective, a novel nonlinear layered shell element, referred to as the Layered Fixed-Strut-Angle Finite Element (LFSAFE) model, was developed and implemented in OpenSees. In this paper, the effectiveness and accuracy of the LFSAFE model is experimentally-validated, via simulation of test results presented in the literature for non-planar (U-shaped and H-shaped) walls specimens subjected to quasi-static multi-directional lateral and torsional loading conditions. Model results obtained for U-shaped wall specimens under uni-directional lateral loading, bi-directional lateral loading, and pure torsion, as well as for H-shaped wall specimens tested under combined lateral and torsional loading, are systematically compared with test results to assess the capabilities of the model. Comprehensive response comparisons provided in this paper demonstrate that the LFSAFE model can accurately simulate salient response attributes of non-planar walls under combined loading, in terms of hysteretic load-displacement and torque-twist behavior, lateral load and torque capacity, stiffness, ductility, as well as contribution of flexural and shear deformations to lateral displacements and the vertical strain distributions developing both along the wall height and across the wall cross section.

Keywords Concrete · Wall · U-shaped · Non-planar · Model · Finite element · Shell · OpenSees · Torsion

Extended author information available on the last page of the article

1 Introduction

Nonlinear response history analysis is the commonly-employed analysis method for seismic performance assessment of existing structures or performance-based design of special structures such as tall buildings. Nonlinear analysis requires efficient modeling methods for simulating the nonlinear behavior of a three-dimensional structural system, and performance-based design/assessment involves comparison of deformation demands obtained from nonlinear dynamic analysis with limits (acceptance criteria) specified in design/assessment codes or supporting documents (e.g. TBI-II 2017; ASCE 41 2023; LATBSDC 2023) corresponding to different performance levels that are targeted in design/assessment. In this context, the performance-based design/assessment approach relies heavily on not only well-documented experimental observations that correlate levels of nonlinear deformations with levels of damage on structural components, but also the use of reliable nonlinear modeling methodologies that can accurately replicate the nonlinear behavioral characteristics of the structural components, as well as their interaction, under complex and multi-directional loading conditions induced by seismic actions on the entire three-dimensional structural system.

Reinforced concrete (RC) structural walls are generally designed as the primary structural components of the seismic-resistant system of building-type structures located in regions of moderate or high seismicity. To date, a considerable amount of experimental research has been conducted and reported in the literature (e.g., see database by Abdullah and Wallace 2018) on planar walls subjected to in-plane loading. Numerous analytical studies have also been conducted on modeling of the nonlinear behavior of planar walls, using either macroscopic (e.g., fiber-based) modeling approaches (e.g., reported by Kolozvari et al. 2018) that do or do not consider nonlinear shear-flexure interaction behavior, or using microscopic (e.g., finite element) modeling approaches (e.g., reported by Kolozvari et al. 2019) that inherently account for coupling of axial/shear/flexural responses of walls. Comparatively fewer experimental campaigns have been conducted to investigate the nonlinear behavior of non-planar RC walls subjected to uni/bi-directional, torsional, or combined lateral-torsional loading conditions (e.g. Habasaki et al. 2000; Ono et al. 2004; Kitada 2007; Beyer et al. 2008a; Li and Li 2012; Constantin and Beyer 2016; Behrouzi et al. 2020; Hoult and Beyer 2021; Hoult et al. 2023a). Non-planar walls with complex cross-sectional geometries are typically used as core wall components in tall building construction, as well as in mid-rise buildings around the perimeter of elevators and staircases. The nonlinear behavior of non-planar walls under seismic actions is significantly more complex than that of planar walls, due to various reasons. First, it has been experimentally-observed (e.g. Constantin and Beyer 2016; Hoult 2019) that plane sections not remaining plane (due to shear lag effects) is more pronounced in non-planar walls subjected to multi-directional lateral loading. As well, shear stresses on non-planar walls migrate across the wall cross section, depending on whether an individual wall segment (e.g., flange) is subjected to axial/flexural compression or tension, where wall flanges subjected to larger axial/flexural compression resist larger internal shear forces, and larger shear deformations/strains develop in flanges subjected to resultant axial/flexural tension (e.g. Beyer et al. 2008a). Furthermore, in buildings that incorporate torsional irregularity, non-planar walls can be subjected to significant torsional demands together with flexural and shear demands. The nonlinear torsional behavior of a non-planar wall is inherently coupled with both its shear and flexural modes of behavior,

since twisting of the wall induces not only shear strains but also longitudinal strains (due to warping) on the wall cross section.

In contrast, industry-standard nonlinear modeling approaches that are commonly used in engineering practice for performance-based design/assessment applications typically do not consider any of these salient behavioral characteristics of non-planar walls. In typical engineering practice, similarly to rectangular or barbell-shaped walls, non-planar walls are modeled using a fiber-based approach, assuming that plane sections remain plane and that the nonlinear flexural behavior of the wall is uncoupled from its shear and torsional responses. Within the framework of performance-based design and assessment, there is clearly a need for adopting improved nonlinear modeling approaches for RC walls, even more so for non-planar walls.

Some of the research studies available in the literature on analytical modeling of non-planar walls, where the models are experimentally-validated against quasi-static test results, are summarized herein. Maruta et al. (1999, 2000a, b) employed a layered shell model element (Hayami et al. 1991) for response simulation of H-shaped walls under combined lateral and torsional loading, focusing on reproducing global load-displacement and torque-twist responses only. Ile and Reynouard (2005) analyzed U-shaped walls under uni- and bi-directional lateral loading, using a three-dimensional multi-layer thin shell finite element formulation. Mazars et al. (2006) validated a multi-fiber beam element modeling approach using test results for a U-shaped wall. Beyer et al. (2008b) developed an inelastic wide-column model formulation and validated it against test results for U-shaped wall specimens. These studies did not include simulation of the torsional behavior of U-shaped walls, and model results were evaluated in terms of global load-displacement behavior only. Lu and Panagiotou (2014) developed a three-dimensional beam-truss model and validated it against test results for three non-planar walls. The beam-truss model was further improved and validated using test results for four planar and four non-planar walls (Lu et al. 2016). These papers also addressed local response prediction capabilities of the beam-truss model, although to a limited extent. More recently Feng et al. (2018) proposed a multi-layer shell element to simulate the nonlinear response of planar and non-planar structural walls. Experimental validation of this model for non-planar walls was conducted mostly at the global load-displacement level, using test results for a T-shaped wall subjected to uni-directional lateral loading, as well as a U-shaped wall tested under bi-directional lateral loads (Constantin and Beyer 2016). Rojas et al. (2019) developed a nonlinear layered shell element, and compared model predictions with test results at both global and local response levels (strains, flexural and shear deformation components) for T-shaped wall specimens loaded uni-directionally. This model has not yet been experimentally-validated for U-shaped walls under bi-directional lateral or torsional loading. Kolozvari et al. (2021a, b, 2022) developed (and implemented in OpenSees McKenna et al. 2000), various modeling approaches for non-planar walls; including a fiber-based nonlinear flexural model, a fiber-based nonlinear shear-flexure interaction model, and single-layer shell model. These models were validated against test results for U-shaped walls tested under bi-directional lateral loading. Modeling of the torsional behavior of non-planar walls was not considered in these studies. Wang et al. (2023) used the finite element analysis software ABAQUS (2016) for modeling of T-shaped and two L-shaped wall specimens they have tested under uni- and bi-directional lateral loading conditions. Model results were compared with test data in terms of the lateral load-displacement response of the wall specimens. In the study by Ahmed et al. (2023), a

nonlinear continuum-type modeling approach was developed and experimentally-validated against test results for non-planar walls subjected to uni- and bi-directional lateral loading. Comparison of model results and test measurements was limited to only the backbone curves of the test results. Hoult et al. (2023b) investigated the effectiveness of the beam-truss modeling approach (Lu and Panagiotou 2014; Lu et al. 2016) in replicating the global load-displacement and torque-twist responses of U-shaped walls tested under uni- and bi-directional lateral loading, as well as pure torsion.

As outlined above, studies in the literature on analytical modeling of non-planar walls, in which the models are experimentally-validated at not only global but also local response levels, against experimental results for wall specimens subjected to various loading conditions, are scarce. The existing level of knowledge on the topic is subject to improvement, in terms of development/validation of a new modeling approach (or validation of an existing modeling approach) for non-planar walls, where the model is extensively validated at both global (load-displacement, torque-twist) and local (shear and flexural deformations, strain distributions) response levels, considering experimental results for wall specimens subjected to uni-directional lateral, bi-directional lateral, torsional, and combined lateral/torsional loading. As well, availability of such a model formulation in open computational platforms would greatly improve modeling capabilities of both researchers and practicing engineers, for conducting more reliable nonlinear response history analysis for (and performance-based design/assessment of) structural systems that incorporate complex non-planar wall configurations.

Accordingly, the objective of this paper is to present a detailed and comprehensive experimental validation study on simulating the hysteretic response characteristics of non-planar RC walls tested under various quasi-static loading conditions, using a new layered-shell model formulation developed and implemented in OpenSees (McKenna et al. 2000) by the authors. The model is referred to as the Layered Fixed-Strut-Angle Finite Element (LFSAFE) model. The companion paper (Tura et al. 2025) presented in this Special Issue provides a detailed description of the model, together with comparison of nonlinear response history analysis results obtained using the model with shake table tests conducted on a U-shaped wall specimen (UWS1, Hoult et al. 2024; Almeida et al. 2024) and the 2015 E-Defense shake table tests conducted on a full-scale ten–story wall/frame building specimen (Sato et al. 2017; Tosauchi et al. 2017; Kajiwara et al. 2017). In the present paper, response simulations obtained using the LFSAFE model are compared with results of carefully-controlled quasi-static tests presented in the literature, conducted on heavily-instrumented non-planar wall specimens subjected to various loading conditions. The test database considered in this paper for experimental validation of the model includes four U-shaped walls tested under uni-directional lateral loading (UW1, Hoult et al. 2023a), pure torsional loading (UW2, Hoult et al. 2023a) and bi-directional lateral loading (TUB, Beyer et al. 2008a; TUC, Constantin and Beyer 2016), as well as with six H-shaped walls tested under combined lateral/torsional loading conditions that correspond to various torque-to-maximum-bending-moment ratios (HW25, HW50, HW75, HS25, HS50, HD25; Maruta et al. 1999, 2000a, b). Model response simulations are compared with test results at both global (e.g., lateral load-displacement, torque-twist) and local (deformation) response levels (e.g., contributions to flexural and shear deformations to top displacement, vertical strain distribution across wall cross-section, vertical strain profile along wall height), in all cases

where local deformation measurements are available. Upon the detailed response comparisons, capabilities and shortcomings of the LFSAFE model are discussed.

2 The Layered Fixed-Strut-Angle Finite Element (LFSAFE) model

The Layered Fixed-Strut-Angle Finite Element (LFSAFE) model is an improved and extended version of the so-called Fixed-Strut-Angle Finite Element (FSAFE) model (Gullu and Orakcal 2021). The baseline FSAFE model element is a single-integration-point and single-layer (membrane-type) element, which has been experimentally-validated against test results for relatively-slender, medium-rise, and low-rise planar walls, as well as T-shaped walls subjected uni-directional lateral loading and U-shaped walls tested under bi-directional lateral loading (see Bilgin et al. 2021; Kolozvari et al. 2022). The FSAFE model element incorporates the so-called Fixed-Strut-Angle Model (FSAM; baseline formulation and experimental validation is presented in Orakcal et al. 2019) as the constitutive plane-stress reinforced concrete panel (membrane) model, where the FSAM was developed based on test results presented in the literature for RC panel (membrane) specimens tested under various stress states and strain histories. The finite element formulation of the 4-node 8-degree-of-freedom (with 2 translational DOFs at each node) of the original FSAFE model could not represent the out-of-plane behavior of a wall or wall segment, since its membrane formulation did not incorporate out-of-plane displacements or rotations. As well, the original FSAFE model element did not include drilling (in-plane rotational) degrees of freedom.

The present LFSAFE model element incorporates a 4-node 24-DOF (3 translation and 3 rotational DOFs at each node) finite element formulation with 9 Gauss integration points. Nonlinear out-of-plane behavior of the model element is based on a thin layered-shell formulation. In-plane strains on the LFSAFE model element are calculated using 3rd-order Hermite shape functions adopted for displacement interpolation, and the corresponding tangent stiffness matrix and restoring force vector is attained via 3×3 Gauss integration. Out-of-plane behavior of the model element is defined using the Discrete Kirchhoff Quadrilateral plate element formulation (Batoz and Tahar 1982). At each Gauss point, nonlinear element behavior corresponding to both the in-plane and out-of-plane (except through-thickness shear behavior) deformation modes are obtained from the in-plane (plane-stress) behavior of the reinforced concrete layers (membranes) comprising the shell element, the constitutive stress-strain behavior of which are represented by the FSAM. Out-of-plane (through-thickness) shear behavior of the thin–shell-type LFSAFE model element is defined as linear elastic. The present formulation of the model element allows simulating nonlinear flexural behavior out-of-plane, whereas it is incapable of simulating nonlinear out-of-plane shear behavior or out-of-plane shear failure.

Formulation of the plane-stress constitutive model FSAM (Fig. 1a), which defines the membrane behavior of each layer in the LFSAFE model element, follows an average strain, smeared stress, and fixed-crack-direction approach, with perfect bond assumed between concrete and reinforcing steel bars. For representing RC panel (membrane) behavior prior to first crack formation, principal stress directions in concrete are assumed to coincide with the principal strain directions of the imposed deformation field on the panel element. When the principal tensile strain first exceeds the cracking strain of concrete, the first crack in the panel model develops, also forming the first concrete “fixed strut”, in parallel direction to

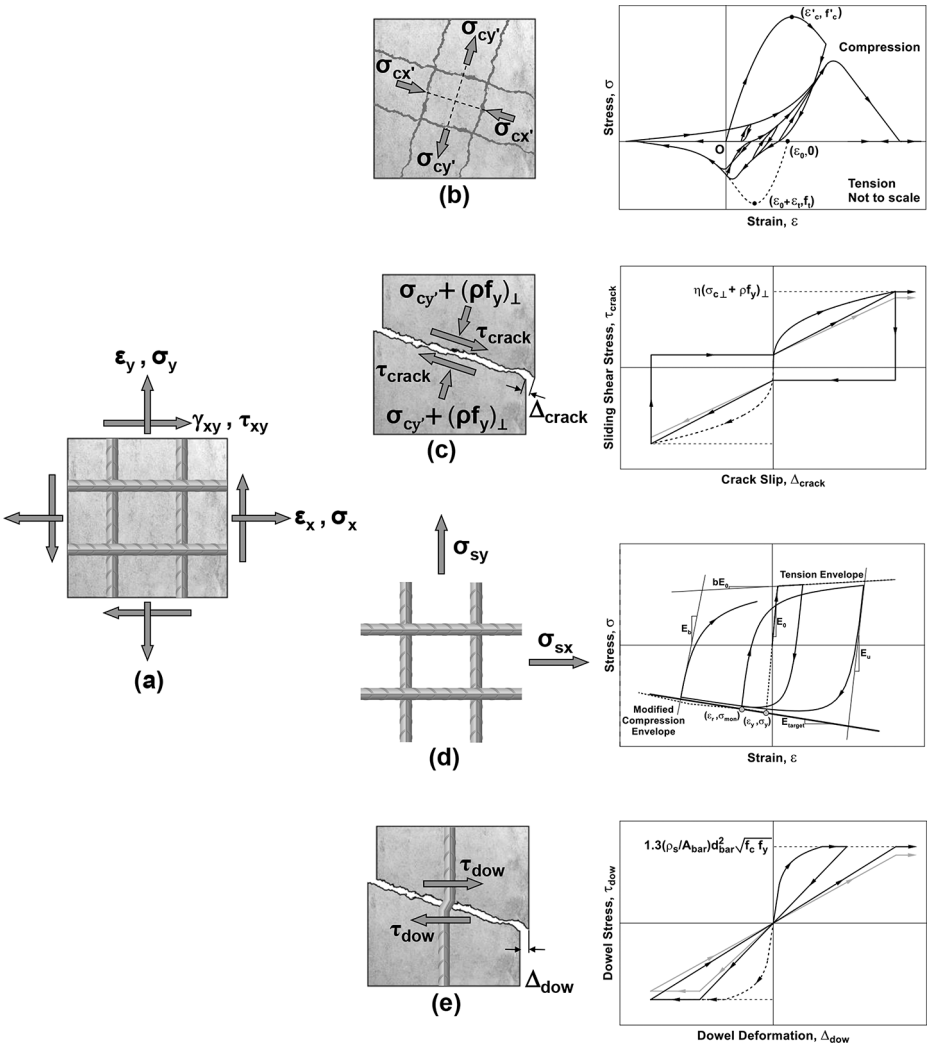

Fig. 1 Constitutive Fixed-Strut-Angle Model (FSAM): (**a**) strain field on RC membrane, (**b**) concrete stresses along fixed struts, (**c**) shear aggregate interlock stresses along crack surfaces, (**d**) uniaxial stresses in reinforcement, (**e**) dowel stresses in reinforcement

the first crack. The applied strain field then is transformed into parallel and perpendicular directions to the first crack, and the second crack in concrete is assumed to develop, forming the second "fixed strut", in perpendicular direction to the first crack, when the tensile strain along the first strut exceeds concrete cracking strain. After formation of the second concrete strut, it is assumed that the two "fixed struts" work in either tension or compression, based on the strain field applied on the panel element (Fig. 1b). Along the two struts with fixed directions, a uniaxial hysteretic constitutive relationship for concrete (Chang and Mander 1994) is adopted. Although the concrete stress-strain relationship adopted in FSAM is fundamentally uniaxial, it also incorporates biaxial softening effects, including compression

softening (Vecchio and Collins 1993) and hysteretic biaxial damage (Mansour et al. 2002), on the uniaxial behavior of the concrete struts. Behavior of reinforcing steel in the two orthogonal reinforcement directions is represented using the uniaxial hysteretic constitutive model by Menegotto and Pinto (1973), as extended by Filippou et al. (1983) to incorporate isotropic strain hardening effects. For longitudinal reinforcement located in wall boundary regions, in order to represent reinforcing bar buckling behavior, the hysteretic constitutive relationship proposed by Dhakal and Maekawa (2002) is adopted in the present model formulation, together with a simplification of the hysteretic rules that neglects the transition regions between the hysteretic loops with the monotonic compression and tension envelope (Fig. 1d). Tension stiffening effects on wall longitudinal reinforcement are also considered in the model formulation, using the relationships proposed by Belarbi and Hsu (1994) for the tensile yield strength and strain hardening ratio of reinforcing steel bars embedded in concrete.

In the constitutive FSAM, for representing shear stress transfer across the fixed cracks, shear stresses developing along the crack surfaces are calculated using a simple friction-based constitutive relationship, and are superimposed with the concrete stresses along the struts in order to obtain total stress field in concrete. The friction-based constitutive relationship representing shear aggregate interlock along crack surfaces relates the maximum shear stress developing along a crack surface to the compressive stress in concrete strut in perpendicular direction to the crack, through a friction coefficient. A smeared "clamping stress" created by the perpendicular component of the yield strength of the reinforcement straddling the crack, is also considered in the compressive stress to be multiplied with this friction coefficient. In order to describe this friction-based constitutive relationship, the monotonic envelope and a simplified version of the hysteresis rules first developed by Tassios and Vintzēleou (1987) and later adopted by Vassilopoulou and Tassios (2003) for rough crack surfaces, is adopted (Fig. 1c). Furthermore, contribution of dowel action on both the horizontal and vertical reinforcing bars on the shear stress field developing on the panel element is incorporated in the model formulation, via adopting the smeared-stress-strain constitutive modeling approach proposed by He and Kwan (2001), together with the dowel force vs. deformation monotonic envelope developed by Vintzēleou and Tassios (1986), 1987) and later adopted by Vassilopoulou and Tassios (2003), and simplified origin-oriented unloading and reloading rules for describing hysteretic behavior (Fig. 1e). It must be mentioned that when large-magnitude dowel deformations develop on reinforcing steel bars, such as those associated with sliding shear behavior/failure along continuous cracks in RC walls (e.g., along a major diagonal crack or a wall-foundation interface crack), the constitutive model adopted in the constitutive FSAM formulation may not realistically represent the hysteretic dowel behavior of reinforcement. However, the LFSAFE model presented in this study is incapable of simulating formation of a single continuous crack on a RC wall, and development of large sliding shear (crack slip) deformations along that crack. The constitutive relationship approach adopted for dowel action in the present model formulation assumes small dowel deformations.

Finally, the resultant average (smeared) stress field developing on the panel element corresponding to the applied strain field, is obtained via superposition of uniaxial concrete stresses developing along the two fixed strut directions, with shear stresses developing along crack surfaces and smeared uniaxial and dowel stresses developing in the horizontal and vertical reinforcement (Fig. 1a). Formulations of the FSAM constitutive model and

the LFSAFE model element are described in more detail in the companion paper (Tura et al. 2025). The LFSAFE model element is implemented in the open–source computational platform OpenSees (McKenna et al. 2000), and will be made publicly-available as soon as possible.

3 Wall test programs used for model validation

Experimental validation of the LFSAFE model was conducted using a wall test database that includes a total of ten non-planar wall specimens tested as part of three different experimental campaigns. The wall specimens selected for model validation were all tested under different loading conditions and they showed a broad spectrum of failure modes during testing. The four U-shaped wall specimens in the database, which were tested by Hoult et al. (2023a) Beyer et al. (2008a), and Constantin and Beyer (2016), were subjected to uni-directional lateral, bi-directional lateral (diagonal or diagonal/sweep), and pure torsional loading conditions. The six H-shaped wall specimens tested by Maruta et al. (1999, 2000a, b) were subjected to combined lateral/torsional loading, with different maximum-bending-moment-to-torque ratios enforced during the tests. Table 1 summarizes some of the important characteristics of all the U-shaped and H-shaped wall specimens, including their dimensions, loading conditions, material strengths, axial load levels, as well as their experimentally-observed behavior and failure modes. Figure 2 illustrates the cross-sections and reinforcement details of the wall specimens.

Specimens UW1 and UW2 were half-scale wall prototypes, and had identical cross-sectional dimensions and almost identical reinforcement configurations, as shown in Fig. 2a. The test setup used for specimens UW1 and UW2 included two horizontal actuators in N–S direction, together with three vertical actuators that were attached to a U-shaped RC collar beam at the top of the wall units (Fig. 3a). The horizontal actuators were used to apply uni-directional lateral loading on specimen UW1, and pure torsional loading on specimen UW2, where the lateral top displacement in N–S direction and the top twist rotation at the elevation of the actuators were controlled during the quasi-static tests of specimens UW1 and UW2, respectively. The three vertical actuators were used to apply constant axial load on the wall units, as well as an additional overturning moment at the top of specimen UW1, for increasing the shear span in the loading direction. For specimen UW1, the shear-span to depth ratios enforced during testing (7.51 in N to S direction, 5.43 in S to N direction) were significantly higher than the aspect ratio of the specimen (1.91), due to the additional overturning moment applied by three vertical actuators. Furthermore, due to the eccentricity between the geometric centroid of the wall cross section and the centroid of the three vertical actuators, the shear span-to-depth ratios in positive (N–S) and negative (S-N) loading directions also differed slightly. On Specimen UW2, together with the constant and concentric axial load applied in an identical manner, pure torsional loading was applied in the form of two forces in opposite directions applied by the horizontal actuators. The experimentally-observed behavior of specimen UW1 specimen was predominantly flexural, where failure of the specimen occurred due to crushing of concrete together with buckling of longitudinal reinforcement (followed by post-buckling rupture upon load reversal) in the south-west boundary region of the wall (Fig. 4a). It is important to note that, a construction defect, which involved off-center placement of the boundary-region reinforcement cage (as

Table 1 Characteristics of test specimens

Specimen ID	Loading Type	h_w (mm)	t_w (mm)	l_w (mm)	$\frac{h_w}{l_w}$	$\frac{M}{Vl_w}$	f'_c (MPa)	$f_{y,BE}$ (MPa)	$\rho_{v,BE}$ (%)	$\rho_{h,web}$ (%)	$\rho_{v,web}$ (%)	$\frac{P}{A_g f'_c}$	Behavior Mode	Failure Mode (1)
UW1	Uni-directional Lateral	2000	100	$1050^{N–S}$ $1300^{E–W}$	$1.91^{N–S}$ $1.54^{E–W}$	$5.43^{S–N}$ $7.51^{N–S}$	38.2	580	2.45^{Edge} 2.18^{Corner}	0.38	0.38	0.050	Flexure	CC/ RB/ LI
UW2	Pure torsion	2000	100	$1050^{N–S}$ $1300^{E–W}$	$1.91^{N–S}$ $1.54^{E–W}$	-	37.1	580	$2.60^{SE-Edge}$ $2.45^{SW-Edge}$ 2.18^{Corner}	0.38	0.38	0.050	Torsion (Flexure-shear)	LI/ OOPS
TUB	Bi-directional lateral	2720	100	$1050^{N–S}$ $1300^{E–W}$	$2.59^{N–S}$ $2.09^{E–W}$	$2.81^{N–S}$ $2.58^{E–W}$	54.7	471	2.45^{Edge} 1.88^{Corner}	0.45	0.38	0.040	Flexure-shear	WC/ DC
TUC	Bi-directional lateral	2720	100	$1050^{N–S}$ $1300^{E–W}$	$2.59^{N–S}$ $2.09^{E–W}$	$2.81^{N–S}$ $2.58^{E–W}$	42	$563^{Corner/Edge}$ 529^{Corner}	$1.34^{SE-Edge}$ $2.45^{SW-Edge}$ $1.25^{NE-Corner}$ $1.15^{NW-Corner}$	0.45	$0.31^{W-Flange}$ $0.91^{E-Flange}$ 1.0^{Web}	0.060	Flexure-shear	FB/ CC
HW25	Combined lateral-torsional	1200	80	880^{Strong} 800^{Weak}	1.36^{Strong} 1.50^{Weak}	1.22–6.73	57.9	403	4.91	0.71	0.71	0.011	Flexure-torsion	CC
HW50						0.98–1.15	57.8					0.011		CC
HW75						0.84–0.86	64.1					0.010		CC
HS25						0.75–1.78	57.6					0.011		-
HS50						0.75–1.78	57.9					0.011		-
HD25						0.75–1.13	62.5					0.010		CC

(1) CC: concrete crushing in flange boundary, RB: reinforcement bar buckling and rupture in flange boundary, LI: lateral instability in flange boundary, FB: out-of-plane buckling of flange boundary, LI/OOPS: lateral instability due to out-of-plane shear in flange boundary; WC/DC: web crushing due to in-plane diagonal compression

reported by Hoult et al. 2023a) impaired effective confinement in this particular wall boundary, which influenced the failure mode of this specimen. For wall specimen UW2, which was subjected to pure torsional loading, the primary behavior mode observed during testing was coupled shear and flexure on individual segments (web and flanges) of the wall, with the applied torque creating not only shear demands on the wall segments, but also giving rise to nonlinear flexural deformations (on especially the wall flanges), associated with warping of the cross-section. For this specimen, onset of concrete crushing was observed at the interior face of the east flange boundary region, leading to localized out-of-plane bending of the region, followed ultimately by lateral instability of the south-east boundary in the out-of-plane direction, due to through-thickness shear effect (Fig. 4b).

The other two U-shaped wall specimens, TUB and TUC, were also half-scale test units with identical cross-sectional dimensions. Reinforcement configurations of specimens TUB and TUC differentiated in terms of longitudinal reinforcement amounts and web-flange intersection boundary region details, as shown in Fig. 2b and Fig. 2c. Both specimens were subjected to bi-directional lateral loading, using three horizontal actuators attached to a U-shaped RC collar beam at the top of the walls, two of which were oriented in the N–S direction of the walls, and the third oriented in the E–W direction (Fig. 3b, c). Specimen TUB was subjected to reversed cyclic loading to increasing ductility levels in N–S, E–W, and diagonal loading directions, followed by a sweep-type top-displacement history at each displacement ductility level. Specimen TUC was tested under reversed cyclic loading in N–S, E–W, and diagonal directions, to increasing drift levels. During both tests, twisting (torsional deformation) of the walls was restrained by two parallel horizontal actuators in N–S direction. Constant axial load was applied using a pre-tensioned tendon that passes through a hollow core jack located on a steel load transfer beam installed at the top of both wall specimens. Both specimens were experimentally-observed to follow coupled flexural/shear behavior throughout testing. Failure mode of specimen TUB (Beyer et al. 2008a) was reported as crushing of concrete under in-plane diagonal compression, in the unconfined region of the wall web (Fig. 4c), whereas failure of specimen TUC (Constantin and Beyer 2016) was correlated with out-of-plane buckling, together with concrete crushing, at the west-flange boundary region of the wall (Fig. 4d).

Experimental validation of the LFSAFE model was lastly conducted against test results for six 1/12-scale H-shaped wall specimens that were tested by Maruta et al. (1999, 2000a, b) under combined lateral and torsional loading conditions. (Fig. 3d). Specimens HW25, HW50, HW75, HS25, HS50, and HD25 had identical geometries and reinforcement configurations (Fig. 2d), but differentiated primarily in terms of the loading condition imposed during testing. The loading setup employed in the test campaign comprised four inclined actuators installed on a stiff steel frame connected to a solid RC block located at on top of the wall units. This loading system was utilized for applying constant axial together with various combined lateral/torsional loading conditions on the wall specimens. During testing of each specimen, the actuator forces were controlled such that the resultant torque applied at the top of each wall is proportional to (i.e., a percentage of) the maximum bending moment developing at base of the wall (i.e., the overturning moment on the wall), for various lateral load directions. The tests were thus characterized by overturning-moment-to-torque ratios imposed on the wall specimens. The nomenclature HS, HW, and HD correspond to resultant lateral load applied in strong, weak, and diagonal directions of the wall cross-section (Fig. 2d), respectively. Specimens HS25, HW25, and HD25 had an overturning-moment-

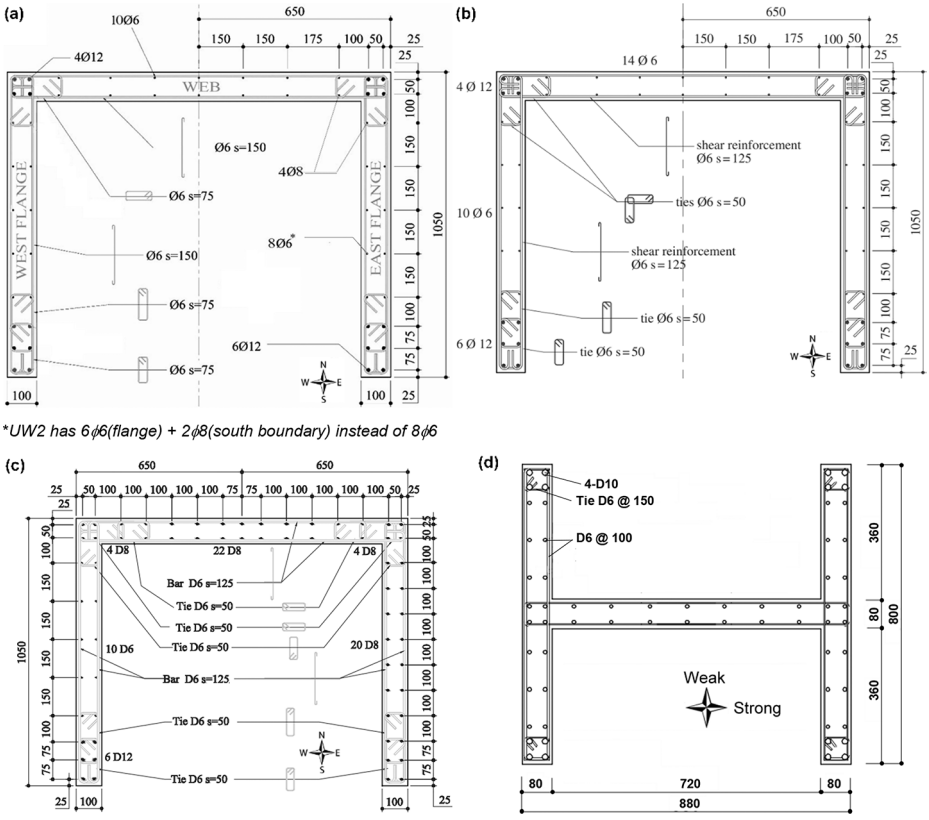

Fig. 2 Wall specimen cross-sections and reinforcement details: (**a**) UW1 and UW2 (Hoult et al. 2023a), (**b**) TUB (Beyer et al. 2008a), (**c**) TUC (Constantin and Beyer 2016), (**d**) H-shaped Specimens (Maruta et al. 2000a). All dimensions are in mm

torque ratio of 3.0 (75% overturning, 25% torque), while specimens HW50 and HS50 had a ratio of 1.0 (50% overturning moment, 50% torque), whereas specimen HW75 had a ratio of 0.33 (25% overturning moment, 75% torque). Shear spans for individual segments (flanges and web) of the walls were defined based on an idealized internal force (shear force under applied torque) distribution assumed for the wall cross-sections, resulting in the broad range of shear span-to-depth ratios listed in Table 1, which are defined for different wall segments under various loading conditions. The experimentally-observed behavior of the H-shaped wall specimens was combined flexural and torsional behavior, where all specimens exhibited flexural/torsional yielding of longitudinal reinforcement. The reported failure mode of the specimens was crushing of concrete at specific wall flange boundaries, due to compressive stresses developing under the combined effects of flexure (flexural compression) and torsion (diagonal compression), except specimens HS25 and HS50 for which significant concrete crushing was not observed.

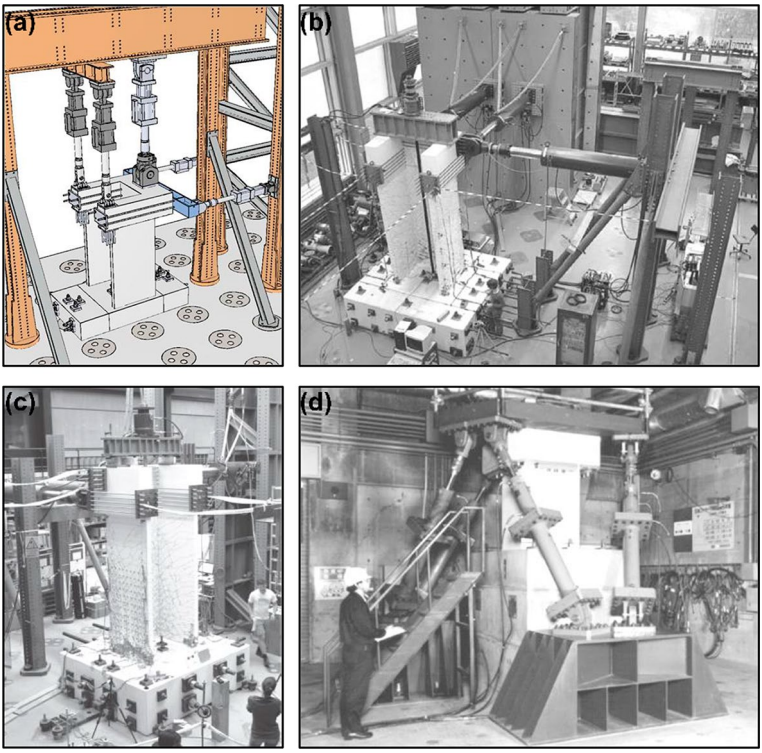

Fig. 3 Test setups for non-planar wall tests; **a**) UW1 (uni-directional lateral load) and UW2 (pure torsion) (Hoult et al. 2023a), **b**) TUB (bi-directional lateral load) (Beyer et al. 2008a), **c**) TUC (bi-directional lateral load) (Constantin and Beyer 2016), and **d**) H-shaped walls (combined lateral load and torsion) (Maruta et al. 2000a)



Fig. 4 Experimentally-observed failure modes: **a**) concrete crushing and out-of-plane reinforcement buckling at flange boundary of UW1 (Hoult et al. 2023a), **b**) out-of-plane shear instability at flange boundary of UW2 (Hoult et al. 2023a), **c**) web crushing of TUB (Beyer et al. 2008a), **d**) out-of-plane buckling of flange boundary of TUC (Constantin and Beyer 2016)

4 Experimental validation of the model

4.1 Geometric calibration, boundary conditions, load application

LFSAFE models for all wall specimens were generated in OpenSees (McKenna et al. 2000), following a unified and consistent approach for discretization of the model geometry and calibration of the material model parameters. Model elements at wall boundary regions were typically discretized along wall length such that the length to thickness ratio of the shell elements do not exceed 2.0, which requires at least two model elements side-by-side for boundary regions with 300 mm length and 100 mm thickness. The model elements are then discretized across the entire wall geometry such that the height-to-length ratios of all elements are close to one. Model element discretization used for modeling of the wall specimens investigated are illustrated in Fig. 5. All wall specimens were discretized along their thickness into nine membrane layers, including two cover concrete layers (unconfined concrete), two horizontal reinforcement layers (horizontal reinforcement and unconfined concrete), two vertical reinforcement layers (vertical reinforcement and confined concrete) and three core concrete layers (confined concrete), as described in Tura et al. (2025).

In all models, both translational and rotational degrees of freedom of base of the walls are restrained, imposing fixed support conditions at wall-foundation interfaces. The geometric constraints enforced at the top of the wall models differ, depending on the respective test set-ups and the loading conditions imposed during the tests. For specimen UW1, the U-shaped RC collar beam is considered as a rigid body constraint at the top of the wall model (since no warping is expected and plane sections are expected to remain plane at the top of the wall), and the additional overturning moment applied at the top of the specimen during testing was enforced as a concentrated moment applied on the rigid body constraint. Axial load on the specimen (as well as the aforementioned eccentricity in axial load) is also applied to the master node of the top rigid body constraint, which is located at the geometric centroid of the wall cross-section. The elevation difference between the top of the wall model and the locations of the horizontal actuators is also considered in the loading conditions imposed on the model. On the other hand, for modeling of specimen UW2, only a rigid diaphragm

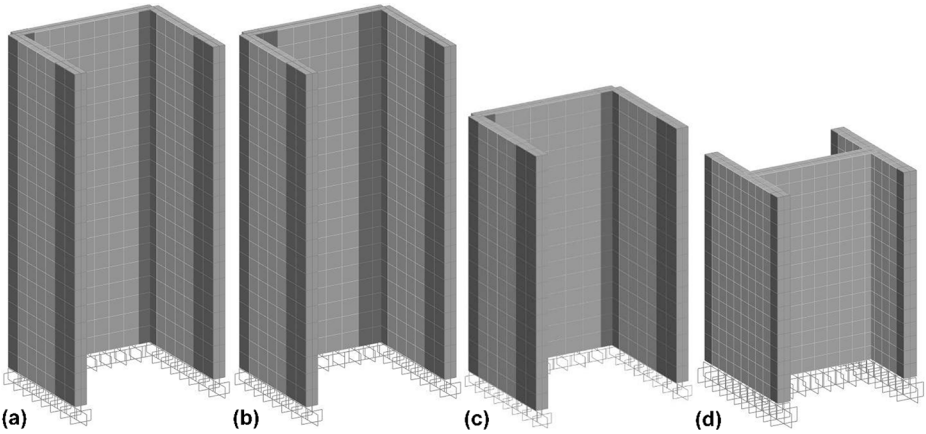

Fig. 5 Model element discretization used for non-planar wall specimens: **a**) TUB, **b**) TUC, **c**) UW1 and UW2, and **d**) H-shaped walls

constraint is enforced at the top of the wall model, so that possible warping of the wall cross-section under pure torsional loading is not fully restrained. Therefore, axial load is applied as distributed point loads at top nodes of the wall model, creating the same axial load resultant (in terms of magnitude and location) applied during testing. Partial restraint against warping of the wall caused by the RC collar beam is considered by modeling of the collar beam using linear elastic frame elements with large flexural stiffness values. However, a cracked torsional stiffness value (i.e., $0.05GJ$) is defined for the middle segment (above the wall web) of the U-shaped collar beam, as discussed in the following section. Differently from specimens UW1 and UW2, the RC collar beams located at the top of specimens TUB and TUC were modelled as vertical extensions of the wall model, in order to apply the lateral loads at different elevations for the two loading directions (i.e., at the elevations of the N–S and E–W actuators). Individual rigid diaphragm constraints are defined along the web and the two flanges of these wall models, at the corresponding actuator elevations. Axial load enforced on these specimens (using the hollow core jack) is applied on the models, at nodes corresponding the location where steel load transfer beam is supported on the collar beam. Lastly, for the H-shaped walls, the rigid load transfer slab (solid RC block) at the top of the wall specimens is represented by using a rigid body constraint defined at the top of the corresponding wall models. Representative deformed shapes for the walls, which are directly obtained from the analysis results presented in this paper, are shown in Fig. 6. The analytically-obtained deformed shapes clearly reflect the loading conditions and boundary constraints imposed on the wall specimens during testing. It is also interesting to observe that the analytical deformed shapes also show localized out-of-plane bending deformations near the base of some of the walls (e.g., Fig. 6d).

4.2 Calibration of material model parameters

Whenever material test results (e.g., stress–strain curves for unconfined concrete in compression and reinforcing steel in tension) were available, the material model parameters used in the LFSAFE model formulation were calibrated to match the as-tested properties of the materials used in construction of the wall specimens. Material model parameters that could not be experimentally-calibrated (e.g., parameters related to confined concrete, concrete tensile strength, reinforcement buckling, tension stiffening, hysteretic material

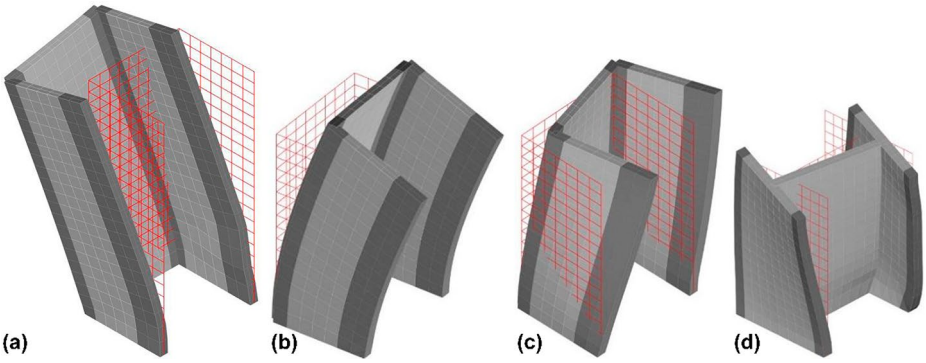

Fig. 6 Representative deformed shapes for non-planar wall specimens: **a**) TUB, **b**) UW1, **c**) UW2, and **d**) HD25

model parameters, shear-friction coefficient on crack surfaces, etc.) were calibrated based on well-established empirical relationships reported in the literature, using a uniform calibration approach used for all wall specimens, as described in the following paragraph. The material model parameters were not adjusted or optimized to match model predictions with test results. As well, in this particular study, it was preferred not to regularize the post-peak compressive stress–strain behavior of concrete depending on model element size (e.g. Coleman and Spacone 2001), in order to assess the accuracy of the model (especially in capturing strength degradation) when a reasonable geometric discretization is adopted and no stress–strain regularization is applied.

In absence of stress–strain test results on concrete, the empirical equations by Chang and Mander (1994) are used to describe the ascending region of the monotonic stress-strain envelope for unconfined concrete under compression. For confined concrete, the ascending region of the stress–strain envelope is defined according to the confinement model by Mander et al. (1988). For both confined and unconfined concrete, the slope of descending region of the stress–strain envelope is calibrated to match the post-peak slope of the Saatcioglu and Razvi (1992) model. Tensile strength of concrete is defined as $f_t = 0.31\ \sqrt{f'_c}$ (MPa) at a cracking strain value of $\varepsilon_t = 0.00008$, as recommended by Belarbi and Hsu (1994) for reinforced concrete membranes. As well, to consider the effect of tension stiffening on the average tensile stress–strain behavior of concrete, the shape of the tension envelope of the Chang and Mander (1994) model is adjusted to match the post-crack average stress–strain relationship proposed by Belarbi and Hsu (1994). The approach proposed by Belarbi and Hsu (1994) for modeling of tension stiffening effects also requires replacing the stress–strain relationship defined for bare reinforcement bars with an average stress–strain relationship defined for bars embedded in concrete, which are expected to be stiffened by concrete between the cracks. This approach is based on the observation that the average tensile strains developing along the length of a RC membrane will be smaller than to the localized tensile strains developing on reinforcing steel bars at crack locations. Accordingly, Belarbi and Hsu (1994) proposed empirical equations for reducing the tensile yield strength and increasing the tensile strain hardening ratio of bars embedded in concrete, based on test results on RC panel specimens loaded uniaxially. Therefore, for all wall specimens analyzed in this study, tensile strength and tensile strain hardening ratio parameters for bare bars are first defined based on material test results reported in respective wall test documents, and these parameters are later modified to reflect the effect of tension stiffening on the tensile behavior of reinforcing bars embedded in concrete, based on the empirical relationships by Belarbi and Hsu (1994). For model elements where reinforcement buckling is not considered (i.e., along unconfined wall regions), in the hysteretic Menegotto and Pinto (1973) model, steel yield strength and strain hardening ratio parameters under compression are taken identical to those for bare bars under tension. In model elements representing the confined boundary regions of the walls, to consider buckling of longitudinal reinforcement, the monotonic envelope parameters and hysteresis rules defined in the Dhakal and Maekewa (2002) model are directly adopted. A slight simplification is made on the hysteresis rules of the Dhakal and Maekewa (2002) model, where the linear transition regions that are used to merge the hysteretic loops with the monotonic compression and tension envelopes are neglected. In both the Menegotto and Pinto (1973) and Dhakal and Maekawa (2002) models, the cyclic stiffness degradation parameters are defined as $R_0 = 20$, $a_1 = 18.5$, and $a_2 = 0.15$.

To represent shear aggregate interlock along crack surfaces, the monotonic envelope parameters and the hysteresis rules developed by Tassios and Vintzēleou (1987) for rough

crack surfaces, are directly implemented. However, the interlock friction coefficient is defined simply as 0.40 (vs. 0.44 recommended by Tassios and Vintzēleou 1987), and the original hysteresis rules are slightly simplified (Fig. 1c). For simulating dowel action on both vertical and horizontal reinforcing bars, the smeared stress-strain constitutive modeling approach developed by He and Kwan (2001) is adopted, together with the monotonic envelope parameters and the hysteresis rules proposed by Vintzēleou and Tassios (1986), 1987). However, the hysteresis rules are slightly simplified into origin-oriented unloading and reloading rules (Fig. 1e). Cyclic degradation effects on the shear aggregate interlock and dowel stresses are also taken into account, using the degradation parameters described in Tassios and Vintzēleou (1987), Vintzēleou and Tassios (1986), and Vassilopoulou and Tassios (2003), also considering later modifications proposed by Thermou et al. (2014).

4.3 Model validation for U-shaped walls under uni-directional lateral loading and pure torsional loading

In order to demonstrate the capabilities and assess the accuracy of the LFSAFE model in simulating the experimentally-observed quasi-static responses of non-planar walls, test results reported by Hoult et al. (2023a), for two U-shaped wall specimens, one tested under uni-directional lateral loading (specimen UW1) and the other tested under pure torsion (specimen UW2) were first compared with model results. Preliminary analysis results obtained for specimen UW1 showed that the construction defect at the southwest boundary region of the wall, in the form of an off-center confined rebar cage and a reduced confined concrete area, had a notable effect in on the failure mode of the specimen (concrete crushing and reinforcement buckling at the southwest boundary), as well as the associated degradation in lateral load at negative 2% drift ratio. In the model, concrete at the southwest boundary region of specimen UW1 was assumed to be unconfined, as the simplest approach for representing the disrupted confinement mechanism in this region. Comparison of the experimentally-measured and analytically-obtained lateral load vs. top displacement responses for this specimen (Fig. 7a) shows that the LFSAFE model successfully predicts the lateral load capacity of the wall in both loading directions, as well as the drift capacity of the wall in the negative loading direction. The hysteretic response characteristics of the wall, including unloading stiffness values, cyclic stiffness degradation, and pinching behavior are also well-represented in the analysis results. The model successfully captures the experimentally-observed strength degradation (degradation in lateral load) at negative 2.0% drift, associated with concrete crushing and reinforcement buckling (Fig. 4a) at the southwest boundary region with the aforementioned construction defect. However, the successive lateral load degradation during the last loading cycle to positive 2.5% drift is not replicated in the model results, since that degradation stemmed from post-buckling rupture of the southwest boundary longitudinal bars upon load reversal, while reinforcement rupture is not considered in the constitutive model formulation adopted for reinforcing steel. It must be mentioned that a hypothetical model configuration where the construction defect at the southwest boundary region of the wall specimen was neglected, provided a nearly identical lateral load–displacement response prediction for the wall, with the exception that the experimentally-observed lateral load degradation at negative 2% drift was not reflected in the analysis results.

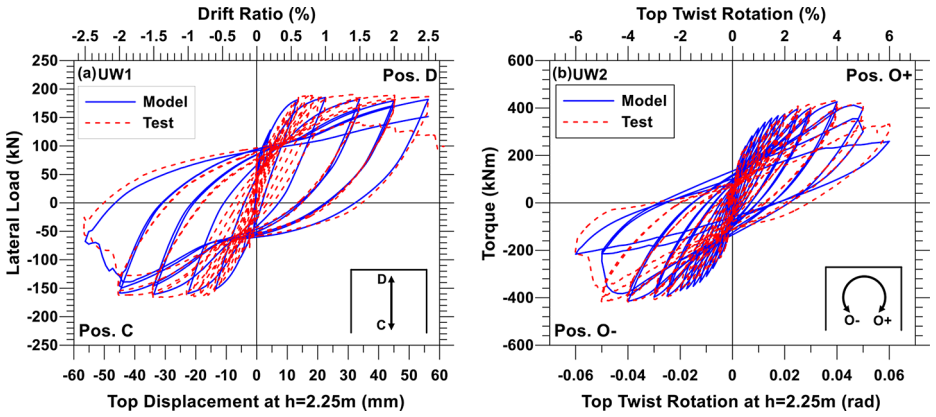

Fig. 7 (**a**) Lateral load vs. top displacement response of specimen UW1, (**b**) torque vs. top twist rotation response of specimen UW2

When the torque vs. top twist rotation response of wall specimen UW2 was simulated, it was observed that model predictions for the torque capacity and twist rotation capacity (prior to torque degradation) of the wall were sensitive to the stiffness properties assumed for the U-shaped RC collar beam located at the top of the wall, due to its restraining effect against warping along the wall cross-section under torsion. In the final model configuration, the collar beam was represented using linear elastic frame elements connected to the top nodes of the wall model, where the stiffness properties of the frame elements were adjusted to represent the expected behavior of the beam segments. First, large axial and flexural stiffness values were defined ($1000AE$ and $1000EI$, where E is the concrete elastic modulus) for all three frame elements used for modeling of the U-shaped collar beam, enforcing the wall cross-section at the top to remain plane. Next, the torsional stiffness of the middle segment of the collar beam (the segment located at the top of the wall web) was reduced, since the torsional stiffness of this middle segment was found to be the main source of the warping restraint (restraint against warping of the wall flanges relative to the wall web) exerted by the collar beam on the wall. Photographs of the wall specimen at the end of the test showed diagonal cracks on the web segment of the collar beam (Hoult et al. 2023a), which is believed to associated with this phenomenon. Since the torsional stiffness of reinforced concrete beams is expected to significantly decrease upon torsional cracking (e.g., $0.05GJ$; Bruun et al. 2020), a stiffness coefficient of 0.05 was used to reduce the torsional stiffness of the middle segment of the U-shaped collar beam. With this configuration, analysis results obtained using the LFSAFE model show that the model successfully predicts the torque capacity and the hysteretic torque–twist angle response characteristics of wall specimen UW2 under pure torsion (Fig. 7b). The experimentally-observed failure mode of the wall was reported as crushing of concrete, together with localized out-of-plane bending, followed by out-of-plane (through-thickness) shear failure of the flange boundary regions (Fig. 4b). Although the LFSAFE model formulation neither considers through-thickness nonlinear shear behavior nor incorporates geometric nonlinearity effects for simulating out-of-plane instability, the model reasonably captures the experimentally-observed degradation in the applied torque and therefore the twist rotation capacity (approximately 5%) of the

wall specimen due to the analytically-estimated concrete crushing and reinforcement buckling of in the wall flange boundary regions.

For wall specimen UW2, in order to demonstrate the influence of the warping restraint imposed by the U-shaped RC loading collar at the top of wall on the analysis results, Fig. 8 compares the experimentally-measured torque vs. top twist rotation response of the wall with model predictions for two extreme cases: (*i*) when the collar is assumed to provide no restraint against warping of the wall cross-section (i.e., a collar beam is not included in the wall model), and (*ii*) when the collar beam in the wall model is assumed to be fully rigid. As can be observed in the figure, when the U-shaped collar beam is not included in the model generated for the wall specimen, the analytically-predicted torque capacity reduces to 340kN.m (versus the experimentally-measured capacity of 433kN.m). In contrast, when a fully-rigid collar beam is considered in the analysis, the torque capacity prediction of the model increases to 590kN.m; however, in this case degradation in torque initiates at a smaller top twist rotation (i.e., approximately 0.03 rad).

Restraint against warping impacts the torsional capacity of non-planar walls similarly to how restraint against elongation (i.e., axial growth) would impact their nonlinear flexural capacity. Restraint against warping alters the behavioral mechanisms associated with widening of the torsional cracks and reinforcement yielding, and influences the vertical (axial), horizontal (transverse), and shear stress and strain distributions on the wall. Typically, the warping restraint increases the axial compressive stresses developing in regions of the wall where axial elongation (that would otherwise be associated with warping) is prevented. Due to the inherently-coupled axial/shear behavior of RC membranes, which is considered in the biaxial constitutive model (FSAM) incorporated in the LFSAFE model formulation, redistribution of the axial stresses causes redistribution of the shear stresses developing across wall cross-section also. This is demonstrated in Fig. 9, where for the two extreme cases assumed in Fig. 8 for the collar beam stiffness, analytically-obtained average axial (vertical) stress and average shear stress distributions across the cross-section of specimen UW2 are plotted, at the base, midheight and the top elevations of the wall specimen, at the instant when the analytically-predicted torque capacity of the wall is reached in both cases (i.e., at positive 2.5% top twist rotation). The average axial and shear stresses plotted in Fig. 9 are equivalent (smeared) stresses in concrete, which also include the contribution

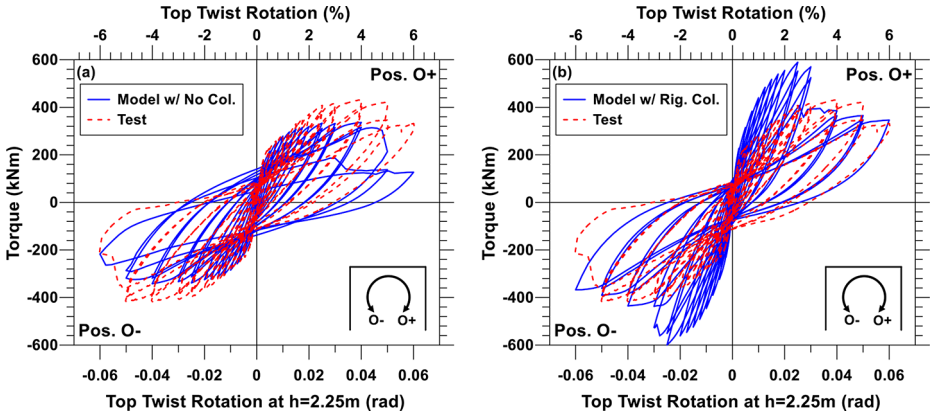

Fig. 8 Influence of collar stiffness on the torsional response predictions for specimen UW2: (**a**) model with no collar beam, and (**b**) model with fully-rigid collar beam

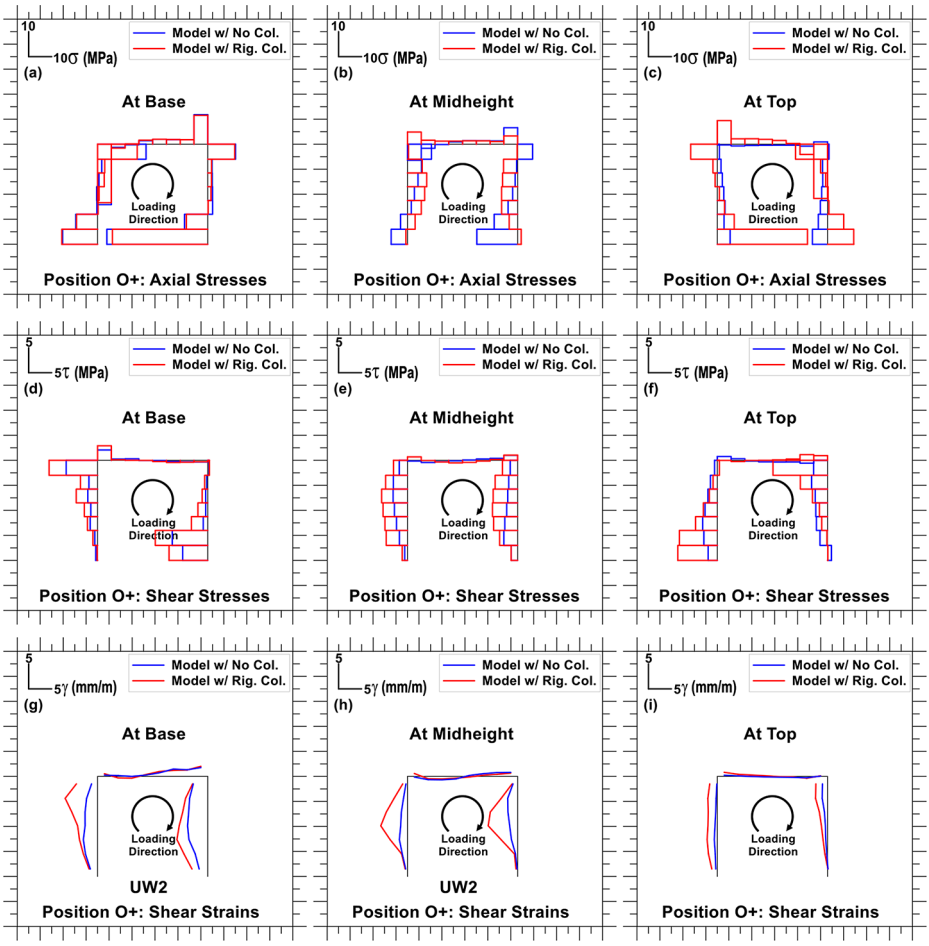

Fig. 9 Influence of collar stiffness (warping restraint) on analytically-obtained average stress and strain distributions for specimen UW2, at positive 2.5% top twist rotation: (**a**), (**b**), (**c**) axial (vertical) stresses, (**d**), (**e**), (**f**) shear stresses, (**g**), (**h**), (**i**) shear strains

of reinforcement. In Fig. 9a, b, c, average axial (vertical) stress magnitudes that fall inside and outside of the lines that represent the wall cross-section correspond to compressive and tensile stresses, respectively. As can be observed in Fig. 9, restraint against warping influences both the average axial stress and the average shear stress distributions on the wall, and consistently causes larger shear stresses to develop across the wall cross-section, which collectively create a larger torque resultant (i.e., torque capacity) for the wall.

In the analytical stress distributions presented in Fig. 9, there is not always a direct correlation between increase in axial compressive stresses with increase in shear stresses at all regions across the wall cross-section. This is because restraint against warping also influences the horizontal normal stress and the vertical/horizontal/shear strain distributions on the wall. In fact, a significant reason why restraint against warping increases the shear stresses on the wall is kinematics. As demonstrated in Fig. 9g, h, i, under the imposed top twist rotation, restraint against warping increases the shear strains developing on the wall,

especially along the flanges of the wall cross-section. This is because individual flanges undergo larger flexural deformations (i.e., larger flexural rotations develop at the top of the individual flanges) when warping is not restrained at the top of the wall. Overall, under the combined influence of these kinematic and behavioral effects, restraint against warping amplifies the shear stresses developing on the U-shaped wall cross-section, resulting in an increased torque resultant/capacity.

At the local response level, the LFSAFE model is first validated against representative experimentally-measured average vertical (longitudinal) strain profiles measured along the height of wall specimen UW1 (Fig. 10). Experimental measurements corresponding to various peak drift levels are obtained from Linear Variable Differential Transformers (LVDTs) attached to the wall at the southwest flange tip (Fig. 10a), southeast flange tip (Fig. 10b), and the northwest web-flange intersection (Fig. 10c). Since the gauge lengths of the LVDTs overlap at the southeast flange tip of the wall, discontinuities (overlaps) in the measured average strains are shown in Fig. 10b, while for all cases, the model predictions are continuous. Model results for the average strains are presented as the Gauss-weighted average of the strain values obtained at the nine Gauss points of each model element. As shown in Fig. 10a, for this particular specimen, the model significantly underestimates the compressive strains measured at the tip of the southwest flange, especially along the first quarter of the wall height. However, this is not deemed to be a characteristic attribute of the model, as such discrepancy is not observed in comparison of model predictions with test measurements for other U-shaped wall specimens, as will be discussed in the following sections. At all drift levels, the model provides reasonable estimations for the tensile strain profiles measured along tip of the southeast flange, (Fig. 10b), and the compressive strains measured along the corner of the northwest web-flange boundary (Fig. 10c).

For wall specimen UW2, which was tested under pure torsion, Fig. 11 compares model predictions with test results for the strains on the outmost longitudinal reinforcing steel bars located in the southwest flange tip of the wall. The strains were measured using continuous fiber-optic strain gauges (distributed fiber optic sensors– DFOS) that were attached to the both the inner (close to the inner wall surface) and outer reinforcing steel bars. Detailed information on the DFOS system is provided in the paper by (Hoult et al. 2023c). For comparison, average longitudinal strains measured using LVDTs attached to the flange tips (at mid-thickness) are also shown in the figure. Comparison of results presented in Fig. 11a (inner gauge) and Fig. 11b (outer gauge) demonstrates that, due to its layered-shell formulation, the LFSAFE model is capable of simulating the out-of-plane (through-thickness) strain

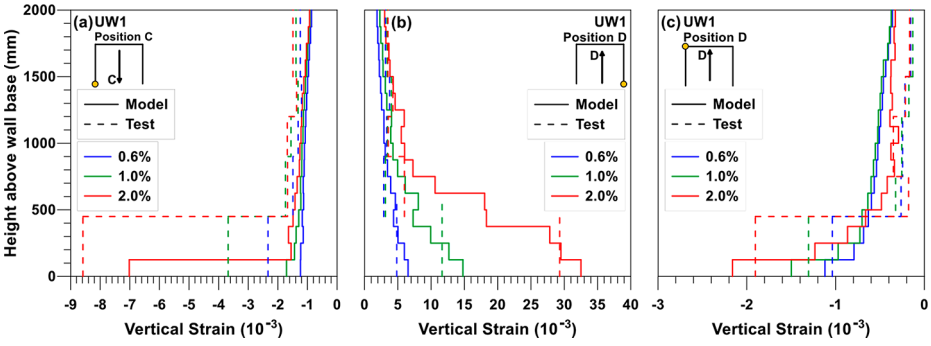

Fig. 10 Vertical strain profiles along wall height for specimen UW1

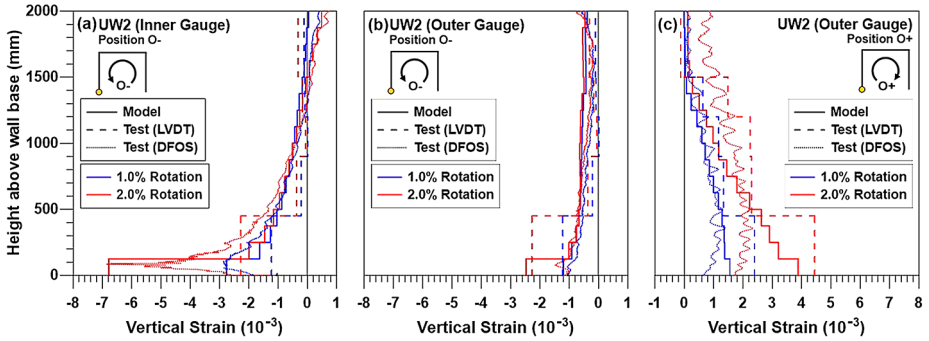

Fig. 11 Vertical strain profiles along wall height for specimen UW2

gradient on the wall. As shown in these two figures, under torsional loading, in both model results and test measurements, compressive strains developing on the inner reinforcing steel bars are larger compared to those on the outer bars. The model provides reasonable predictions of the different magnitudes of compressive strains developing in the inner and outer bars, which is a significant attribute of the model towards simulating out-of-plane instability failures in wall flange boundaries, especially upon future implementation of geometric nonlinearity effects in its formulation. Furthermore, as demonstrated in Fig. 11c, under torsional loading, the model is also reasonably successful in capturing the magnitudes and distribution of the longitudinal tensile strains developing along the wall height, when both LVDT and DFOS measurements are taken into account. Nevertheless, the average tensile strains measured by the 450 mm-gauge-length LVDTs located at the base of the wall are underpredicted by the model (Fig. 11c), primarily due to neglecting strain penetration effects in analysis, as will be discussed later in this paper.

Figure 12 compares model estimations for the distribution of inner-surface longitudinal strains at the base of wall specimen UW2, with experimentally-measured average strain profiles obtained from 60 mm-gauge-length vertical micrometers attached to the inner surfaces of the web and flanges at the base of the wall, under two representative twist rotation levels in both positive and negative loading directions. In Fig. 12, longitudinal strain distributions are presented across both the web and flanges, where the strain magnitudes that fall inside and outside of the lines representing the wall cross-section correspond to compressive and tensile strains, respectively. The magnitudes of the strains are scaled such that each major tick mark on the horizontal and vertical axes of the plots corresponds to a strain magnitude of 10 mm/m (1.0%). For example, Fig. 12b reveals that the model predicts approximately 2.0% tensile strain at the southwest flange tip of the wall cross-section, under 3.0% twist rotation in the positive loading direction. As can be observed in Fig. 12, the model significantly underestimates the tensile strains developing on the flanges subjected to torsional tension. The primary reason for this discrepancy is negligence of strain penetration effects in modeling, as will be demonstrated in the following paragraphs. In contrast, tensile strains developing in the web, and both tensile and compressive strains developing in the flanges subjected to torsional compression (as well as transition of these strains from tension to compression) are generally well-represented in the model results.

Longitudinal strain comparisons presented in Figs. 10, 11, and 12 for wall specimens UW1 and UW2 reveal that in some cases (e.g., Fig. 11c, Fig. 12), the model tends to under-

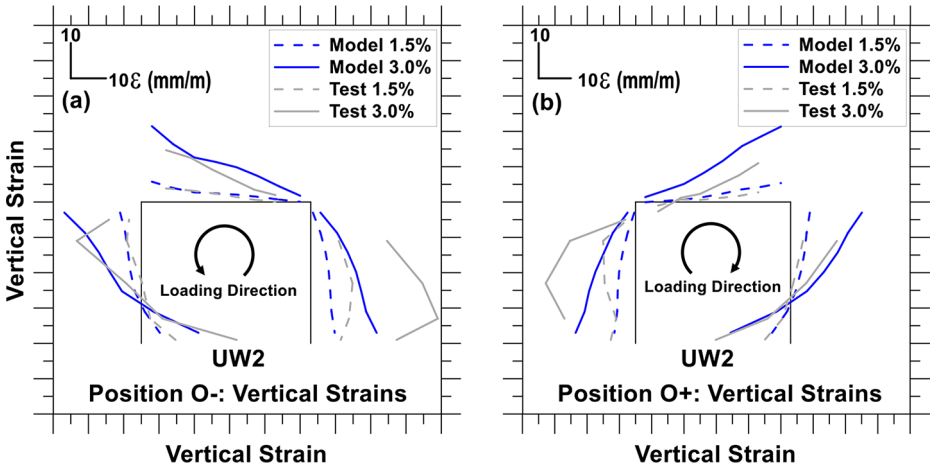

Fig. 12 Vertical strain distributions across wall base for specimen UW2

estimate the average tensile strains measured by the LVDTs or micrometers installed at the base of the wall specimens (i.e., sensors that straddle the wall-foundation interface). Since the foundation of the wall specimens and the strain penetration effects on the longitudinal reinforcing bars in the foundation were not considered in the original model configuration, an updated model configuration was also generated for specimens UW1 and UW2, where strain/yield penetration effects were considered in modeling, using the indirect (macroscopic) approach adopted in the paper by Hoult and Almeida (2024a). The same macroscopic modeling approach was also used in modeling of strain penetration effects on the walls investigated in the companion paper (Tura et al. 2025). In this indirect approach, strain/yield penetration effects (longitudinal bar extension/slip deformations developing within the foundation of a wall and accumulating at the wall-foundation interface) are represented in the form of average tensile strains that are assumed to develop within an additional row of LFSAFE model elements that are defined directly below the wall-foundation interface. The model nodes at the wall-foundation interface are restrained from horizontal displacements, and these row of model elements that represent the foundation are assigned zero concrete tensile strength and approximately linear elastic stress-strain behavior for concrete in compression. For specimen both specimens UW1 and UW2, the height of these additional model elements (i.e., the strain penetration depth) is defined as 220 mm, as recommended by Hoult et al. (2022) based on strain gauge measurements taken from the longitudinal bars extending into the foundation of these walls.

Fig. 13 compares model predictions for the vertical (longitudinal) tensile strains at the base and along the height of wall specimens UW1 and UW2, obtained using both the original and updated model configurations, with LVDT and DFOS measurements. In Figs. 13a and 13b, for easier comparison with LVDT measurements (i.e., for compatibility with the LVDT gauge lengths), model predictions for the average vertical tensile strains developing along the bottom 600 mm and 500 mm height of walls UW1 and UW2 are plotted, respectively. Fig. 13a reveals that for wall specimen UW2, consideration of strain penetration effects slightly improves the model predictions for the average vertical tensile strains measured by LVDTs at the base of the southeast flange tip of wall. However, as shown in

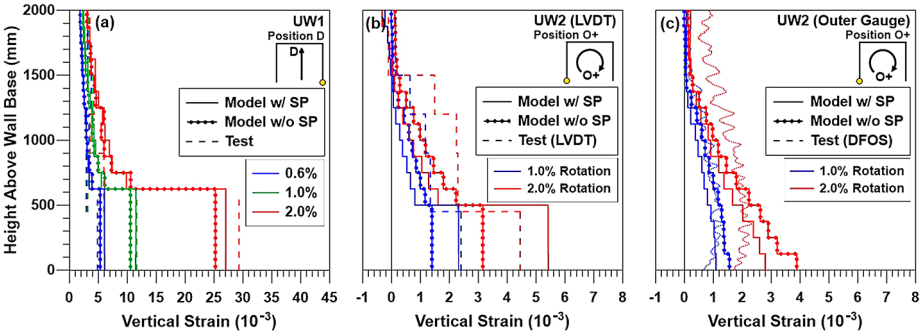

Fig. 13 Influence of considering strain penetration effects on vertical tensile strain predictions for specimens UW1 and UW2

Fig. 13b, consideration of strain penetration effects improves, more significantly, the average vertical tensile strain predictions of the model at the base of the southwest flange tip of specimen UW2. Also for specimen UW2, as depicted in Fig. 13c, consideration of strain penetration effects leads to a reduction in the model predictions for the tensile strains developing in an outer-layer reinforcing steel bar located at the southwest flange boundary region of the wall, which brings them closer to those measured by the DFOS installed on the bar. This is expected, since both model predictions and test measurements shown in Fig. 13c are closer by definition to actual material strains (versus average strains defined along LVDT gauge lengths), and do not incorporate the strain penetration (extension/slip) deformations that are concentrated at the wall-foundation interface.

For wall specimen UW2, the original model configuration was shown in Fig. 12 to significantly underestimate the average longitudinal (vertical) tensile strains developing on the wall flanges subjected to torsional tension, compared to those measured by the micrometers installed on the inner-surface of the wall, at the base. Therefore, Fig. 14 compares predictions of the updated model for the average vertical strains distributed across the wall cross-section at the base of the wall, with the experimentally-measured average vertical strain profiles. As can be observed in Fig. 14, the updated model configuration, where strain penetrations effects are indirectly considered in analysis, provides improved predictions (compared to Fig. 12) for the vertical tensile strain distributions on the wall flanges subjected to torsional tension, while the average tensile strain predictions of the model at other locations on the wall cross-section, as well as the average compressive strain predictions of the model, are not significantly influenced or impaired. Overall, indirect consideration of strain penetration effects in the analysis, is found to notably improve the average vertical strain predictions of the model, particularly at the base of the torsionally-loaded wall specimen UW2.

Finally, global response predictions of the updated model (in which strain penetration effects are considered) for the lateral load vs. top displacement response of wall specimen UW1, as well as the torque vs. top twist rotation response of specimen UW2, are compared with test measurements in Fig. 15. Compared to the original model results shown in Fig. 7, results presented in Fig. 15 reveal that incorporating strain penetration effects in the analysis (with the macroscopic modeling approach adopted) does not significantly influence the model predictions for the lateral load vs. top displacement or the torque vs. top twist rotation of these particular wall specimens, other than a slight increase in the analytically-predicted

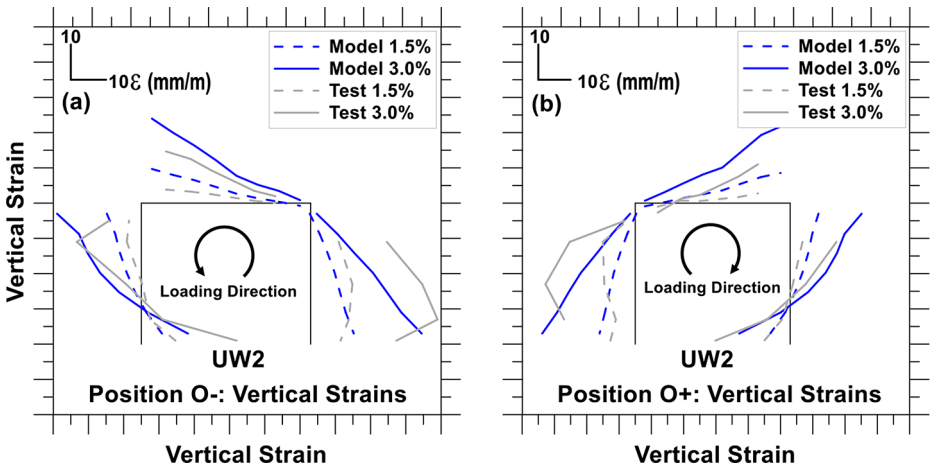

Fig. 14 Vertical strain distributions across wall base for specimen UW2 when strain penetration effects are considered in modeling

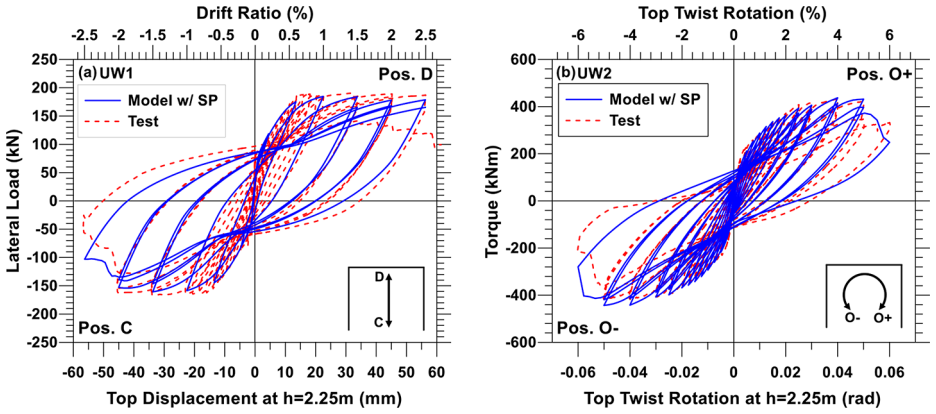

Fig. 15 Global response predictions when strain penetration effects are considered in modeling: (**a**) Lateral load vs. top displacement response of specimen UW1, (**b**) Torque vs. top twist rotation response of specimen UW2

twist rotation capacity for specimen UW2 (Fig. 7b vs. Fig. 15b). It is believed that strain penetration effects are more influential on the wall response especially when a continuous crack develops at the wall-foundation interface. In the absence of a continuous interface crack, possibly due to the slowly-applied and carefully-controlled top displacements imposed on wall specimens during quasi-static tests, and especially for relatively slender (i.e., flexible) walls that are also subjected to large flexural/torsional ductility demands, strain penetration effects may not be notably influential on the global response characteristics of walls. However, in cases where continuous wall-foundation interface cracks develop, strain penetration effects may possibly lead to unforeseen failure modes that can adversely affect RC wall response and performance, such as localized and premature crushing failure (i.e., toe crushing) at the base of a wall, as discussed in the Future Challenges section of the

companion paper (Tura et al. 2025). For the remaining wall specimens investigated in this paper, strain penetration effects are not considered in modeling, since the adopted macroscopic modeling approach is not a constituent of the LFSAFE model element formulation.

4.4 Model validation for a U-shaped wall under diagonal/sweep lateral loading

Experimental validation of the LFSAFE model is further conducted for wall specimen TUB (Beyer et al. 2008a), which was subjected to a complex multi-directional lateral load history. Figure 16a (in E–W direction), Fig. 16b (in N–S direction), Fig. 16c,d (along diagonal direction), and Fig. 16e (square-root-of-sum-of-squares) compare the lateral load–top displacement response predictions of the LFSAFE model with experimentally-measured responses. In order to directly replicate the complex loading protocol shown in Fig. 16f, a multi-directional (multi-DOF) displacement controlled nonlinear analysis solution strategy was first implemented into OpenSEES. The baseline formulation of this strategy is described in the thesis by Bilgin (2018). The experimentally-measured lateral displacements on the wall specimen at 2.95 m elevation were applied to the analysis model, controlling the lateral displacements in E-W and N–S directions at the northeast corner, and in N–S direction at the northwest corner of the wall model cross-section. Similar to the manner as to how torsional twisting of the specimen was restrained during testing, the same displacement history in the N–S direction was applied at the northeast and northwest corners of the analysis model, preventing any twist rotation at the top. Furthermore, since the horizontal actuators were attached to the wall specimen at different elevations (N–S at 2.95 m, E-W at 3.35 m), the horizontal forces used in the displacement-controlled analysis were defined at the same elevations of the actuators, although lateral displacements were controlled at an elevation 2.95 m.

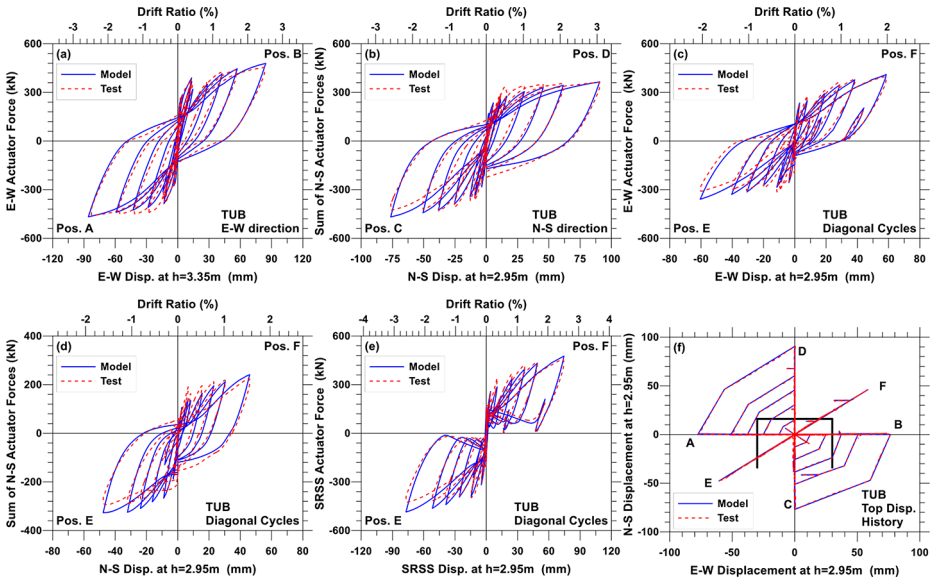

Fig. 16 Lateral load vs. top displacement responses for specimen TUB

The lateral load–top displacement response comparisons presented in Fig. 16 along various loading directions demonstrate that the LFSAFE model is capable of simulating, with reasonable accuracy, the backbone (stiffness, yield load and displacement, maximum lateral load, and strain hardening) characteristics; as well as the hysteretic (unloading stiffness, hysteretic stiffness degradation, and pinching) characteristics of the experimentally-measured response of wall specimen TUB. For this wall, degradation in lateral load was not observed either in test measurements or in model response predictions. The observed failure mode of this specimen was reported as concrete crushing along the base of the wall web under diagonal compression; however, it did not create any strength loss, possibly due to redistribution of compressive stresses. In general, the only discrepancy between model predictions and test results is that whenever the applied lateral load incorporates a N–S component, the model slightly underestimates the experimentally-measured lateral loads during the initial loading cycles in the positive loading direction (at positions D and F) and slightly overestimates the lateral loads during the final loading cycles in the negative loading direction (at positions C and E). The load–displacement response of the wall during the uni-directional loading cycles (Fig. 16a and Fig. 16b) is well-simulated. Figure 16c and Fig. 16d present analytical and experimental response comparisons for the E-W and N–S components of the load–displacement response, during the diagonal loading cycles, for which a reasonably accurate response prediction is again obtained. The square-root-of-sum-of-squares (SRSS) resultant of the lateral load vs. top displacement response of the wall presented in Fig. 16e for the diagonal loading cycles (where the resultant lateral load and displacement are not necessarily oriented in the same direction) also show good agreement between model results and test measurements. Last, Fig. 16f illustrates replication of the multi-directional top displacement history imposed during testing, with the multi-directional displacement control solution strategy implemented in OpenSees, which renders OpenSees suitable for conducting quasi-static analysis under such loading conditions without having to define any analysis stages. Overall, the LFSAFE model is shown to be accurate in simulating the global lateral load–displacement response of this specimen, under the complex multi-directional loading history applied during testing.

The experimentally-measured flexural deformation contributions to top displacement of specimen TUB, during the N–S (Fig. 17a), E-W (Fig. 17b), and diagonal (Fig. 17c,d) loading cycles, are used to assess the capabilities of the model in predicting flexural and shear deformations developing along different segments (flanges and web) of non-planar walls under bi-directional lateral loading. The experimental data in the figure does not consider small-magnitude sliding shear deformations that were measured at the base of the wall (with maximum contributions to top displacement of approximately 1.2%, 2.2%, and 4.4% for the web, west flange, and east flange, respectively). Consistently, the present formulation of the LFSAFE model is not capable of simulating formation of a continuous horizontal crack at a wall-foundation interface and shear sliding deformation along that interface crack. Comparisons presented in Fig. 17 reveal that the model slightly overestimates the measured flexural deformation contributions in the flanges of the wall during the N–S loading cycles (Fig. 17a), whereas for the E-W loading cycles, model predictions for the contribution of flexural deformations in web coincide with test measurements (Fig. 17b). During the diagonal loading cycles, the model moderately overestimates the flexural deformation contributions to top displacements in the N–S direction, in both the east and west flanges of the wall (Fig. 17c), while it captures the contributions of flexural deformation in the wall web to top

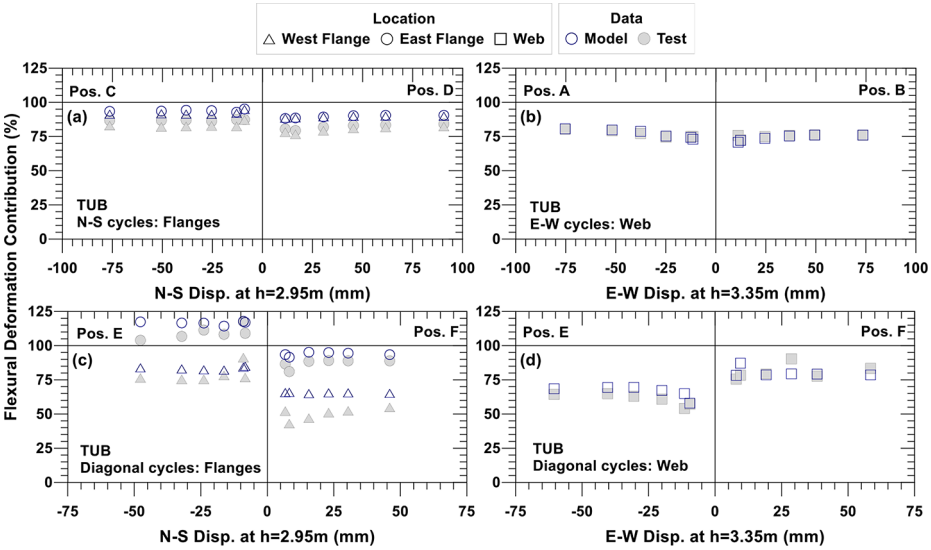

Fig. 17 Flexural deformation contributions to top displacement for specimen TUB

displacements in the E-W direction (Fig. 17d). Results presented in Fig. 17 foremost reveal that the LFSAFE model successfully simulates different intensities of shear-flexure interaction behavior (different levels of shear deformations) in the web and flanges of U-shaped walls under uni- or bi-directional lateral loading. Furthermore, and importantly, as can be observed in Fig. 17c, in both model predictions and test measurements, when a particular wall flange, (e.g., west flange) is subjected to flexural tension due to one component of the bi-directional lateral load, it undergoes higher shear deformation under the perpendicular component of the same lateral load. Results presented in Fig. 17c are also interesting in the sense that in both model results and test measurements, when the east flange of the wall is under flexural compression, the contribution of flexural deformations in the east flange exceed 100% of the top displacement of the wall in N–S direction. A close scrutiny of the model results reveals that this is due to a complicated internal shear flow mechanism developing in the wall under bi-directional loading, where shear deformations (shear strains) and flexural deformations (curvatures) in the flange can add up to lateral displacements in opposite directions. On the whole, the model can be deemed successful in simulating nonlinear shear behavior and shear-flexure interaction in U-shaped walls under uni or bi-directional lateral loading, as well as predicting larger shear deformations in wall segments (e.g., flanges) that are subjected to flexural tensile demands, depending on the sense of the bi-directional lateral load.

Accuracy of the LFSAFE model in predicting the experimentally-measured longitudinal strain distribution along the height of specimen TUB is evaluated in Fig. 18. In the figure, average strain measurements obtained from vertical LVDT's attached to the outer surface of the wall at the flange tip and at the corner of the web-flange intersection, are compared with model estimations. Similarly to specimen UW2, model results for the average strains are calculated as the Gauss-weighted average of the strain values at the nine Gauss points of each model element. The vertical strain profiles are compared at the southwest

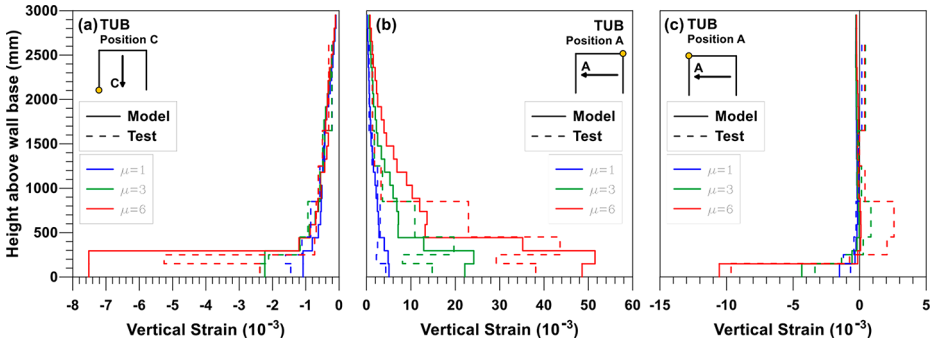

Fig. 18 Vertical strain profiles along wall height for specimen TUB

flange tip (Fig. 18a) at loading position C (under compression), at the northeast web-flange intersection (Fig. 18b) at loading position A (under tension), and the northwest web-flange intersection (Fig. 18c) at loading position A (under compression). Results presented in the Fig. 18a reveal that when the southwest flange boundary is under compression, although the compressive strains measured at the base of the flange boundary are somewhat overestimated by the model at the high displacement ductility level ($\mu = 6$), model predictions for the compressive strains well-match the measured strains at low ($\mu = 1$) and intermediate ($\mu = 3$) displacement levels, along entire wall height. Model estimations for the tensile strains at the base and along the height of the northeast web-flange intersection of the wall are also fairly accurate (Fig. 18b). As depicted in Fig. 18c, when the west flange of the wall is under flexural compression, although the distributions of both the predicted and the measured vertical strains along the height of the northwest web-flange-intersection of the wall are unconventional (mostly due to small strain magnitudes), the compressive strains at the base of the wall are well-predicted by the model at all displacement ductility levels. When the west flange of the wall is under flexural compression (Fig. 18c), the tensile strains measured at the at the northwest web-flange-intersection of the wall (along 300 mm to 800 mm elevation from wall base) are most likely plastic tensile strains (that correspond to compressive stresses) in the reinforcement, which developed upon reversal from larger tensile strains. Similarly to the strain measurements and predictions shown in Fig. 18b for the northeast web-flange intersection of the wall, significant post-yield tensile strains were measured at northwest web-flange-intersection during previous loading cycles in the opposite direction, which the model also underestimated at those elevations (300 mm–800 mm from wall base). As a result, at those elevations, the model was unable to capture the experimentally-measured plastic tensile strains shown in Fig. 18c. Other that this discrepancy, results shown in Fig. 18 showcase the effectiveness of the LFSAFE model in estimating the magnitudes and distribution of compressive and tensile strains developing along the height of U-shaped walls subjected to bi-directional loading, both at flange boundaries and at web-flange intersections.

4.5 Model validation for a U-shaped wall under diagonal lateral loading

Accuracy of the LFSAFE model was further verified by comparing model predictions with experimental measurements for wall specimen TUC (Constantin and Beyer 2016), which

was tested under lateral loading along two diagonal directions. Although specimens TUB and TUC had identical dimensions, reinforcement configurations in the east flange and the web differentiated (see Table 1). As well, the bi-directional loading protocols applied on the two specimens were entirely different. Figure 19 compares model predictions for the lateral load – top displacement response of the wall with test results only for the diagonal loading cycles, since the N–S and E-W loading cycles were applied to small top displacement levels, and the wall specimen was observed to show nonlinear behavior mainly during the diagonal loading cycles. As shown in Fig. 19a, during the diagonal loading cycles in the northwest-southeast direction, the model slightly overestimates the lateral loads capacity and the unloading stiffness characteristics of the E-W component of the wall response, whereas the experimentally-measured lateral load degradation at approximately negative 1.6% E-W drift, is successfully captured. For the same diagonal loading cycles, the model underestimates the N–S component of lateral loads in the positive direction (Fig. 19b). However, in the negative direction, the model accurately simulates the lateral load capacity, drift capacity, and lateral load degradation characteristics of the N–S component of the response (Fig. 19b). As depicted in Fig. 19c, for the northwest-southeast loading cycles, model results obtained for the resultant load–displacement response of the wall, using the SRSS resultant of the N–S and E-W lateral load and displacement components, are again well-representative of the test results, in terms of the lateral load capacity of the wall in both directions, hysteretic response characteristics of the wall, and the drift capacity of the wall (approximately 2.5% SRSS drift) in the negative direction. During the diagonal loading cycles in the northeast-southwest direction, similarly to the previous case, the N-S components of lateral loads in the positive direction (when part of the wall web is under flexural compression) are moderately underestimated by the model (Fig. 19d). However, in the negative direction (when the wall web is under flexural tension), the lateral load capacity, drift capacity, and lateral load degradation characteristics of the N-S component of the response

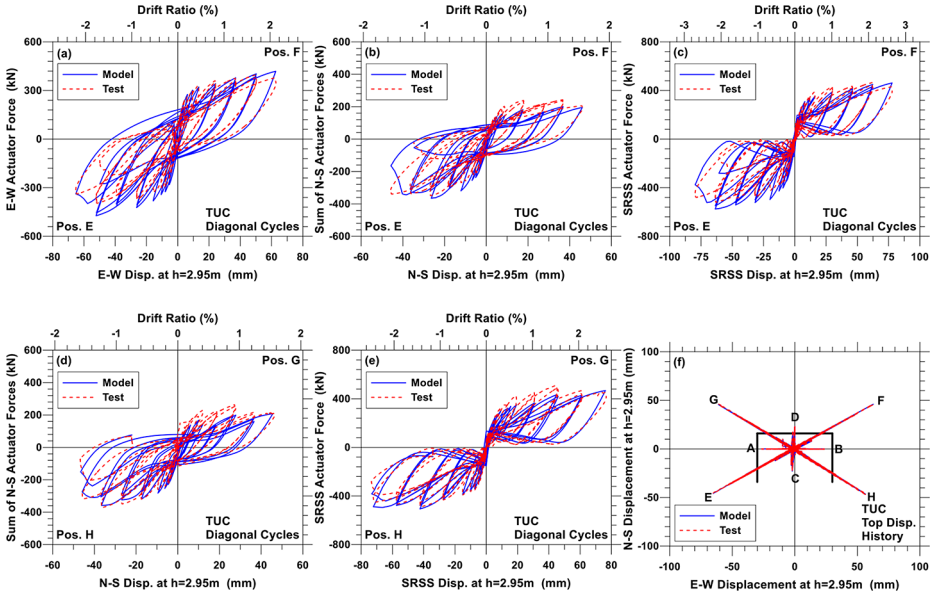

Fig. 19 Lateral load vs. top displacement responses for specimen TUC

(Fig. 19d) are well-predicted. Again, the model provides a reasonably accurate response simulation for the resultant load–displacement response of the wall (Fig. 19e), including the lateral load capacity of the wall in both directions (although slight underestimation is observed in the positive direction), hysteretic characteristics of the response, strength loss during the last loading cycle in the negative direction, as well as the drift capacity of the wall in the negative direction (approximately 2.4% SRSS drift). In summary, other than slight underestimation of the lateral load capacity of the wall when the wall web is under flexural compression (which is subject to improvement upon better definition/calibration of tensile strain hardening behavior in the constitutive model adopted for reinforcing steel), the LFSAFE model can be deemed successful in replicating the overall lateral load–displacement response attributes of U-shaped walls under diagonal lateral loading. Furthermore, the experimentally-observed failure mode of Specimen TUC was out-of-plane buckling of the flange boundary of the wall accompanied by concrete crushing (Fig. 4d). In the analytically-predicted response, out-of-plane buckling of the flange boundary region is not captured since geometric nonlinearity at the model element level is not yet considered in the model element formulation. However, degradation of lateral load in the model results stems from crushing of concrete and buckling of longitudinal reinforcement in the flange boundary regions of the wall, which is somewhat compatible with the experimentally-observed failure mode, since it is also associated with compression failure at flange boundaries.

Figure 20 compares the distribution of longitudinal strains determined from optical sensor measurements on the outer surface of wall specimen TUC, across the wall cross-section at the base of the wall, with model predictions. Strain distributions presented in the figure correspond to loading positions C, F, and H, and are measured at low and intermediate SRSS drift ratios, as test results for larger drift ratios were not available. As can be observed in Fig. 20a, at loading position C, when the web of the wall is under flexural tension under uni-directional lateral load, tensile strains in the central regions of the web are moderately overestimated, although the compressive and tensile strains along the flanges and at the tensile strains at the web-flange intersection regions are well-captured. At loading positions F (Fig. 20b) and H (Fig. 20c), under diagonal loading, when either part of the web is under flexural compression or when the web is under flexural tension, the model well-replicates the highly-nonlinear distribution of the longitudinal strains (i.e., plane sections not remaining plane) across the wall cross section, and well-predicts the magnitudes of tensile strains developing across the entire cross-section as well as the magnitudes of compressive strains developing in flange boundary regions. In this case, the model tends to significantly underestimate compressive strains at the web-flange intersection regions (Fig. 20b). However, this is not believed to be a characteristic shortcoming of the model (e.g., see Fig. 10c and Fig. 18c., where compressive strains at wall web-flange intersections are accurately predicted at even larger drift or displacement ductility levels).

The analytically-predicted average shear stress distributions also shown in Fig. 20 (average of the shear stresses developing in the layers of each model element), clearly demonstrate the migration of shear stresses across the wall cross section, depending on the direction of loading and the resulting distribution of longitudinal strains across the cross-section. Especially in the flanges of the wall specimen, which collectively resist the shear force on the wall cross-section in the N-S direction, the flange subjected to flexural compression is shown to resist the majority of the resultant shear force (Fig. 20b and Fig. 20c). Furthermore, shear stresses developing along a particular flange migrate towards the region

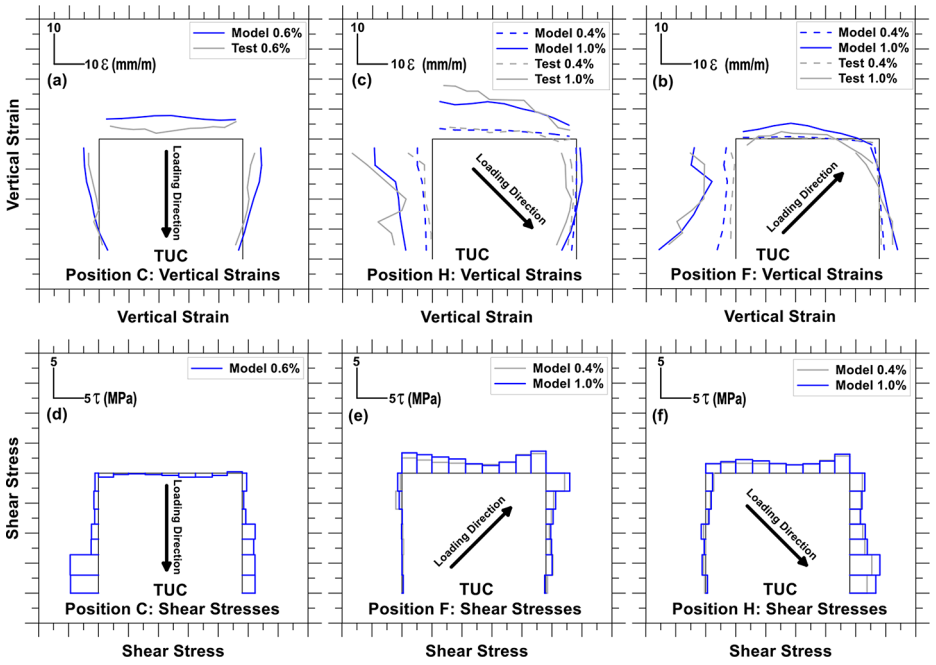

Fig. 20 Vertical strain and shear stress distributions across the wall cross-section at wall base for specimen TUC; **a**) strains at position C, **b**) strains at position F, **c**) strains at position H, **d**) shear stresses at position C, **e**) shear stresses at position F, and **f**) shear stresses at position H

subjected to vertical compressive strains (and therefore axial compressive stresses), since axial and shear stresses are inherently coupled at the model element level. These analytical results demonstrate the capabilities of the LFSAFE model in representing the migration of shear stresses on a wall cross-section towards better-predicting the distribution of the internal shear forces developing in the web and flanges of non-planar walls under multi-directional loading.

4.6 Model validation for H-shaped walls under combined lateral/torsional loading

The final experimental campaign that was used in this study to validate the LFSAFE model is the wall test program conducted by Maruta et al. (1999, 2000a, b) on H-shaped wall specimens subjected to combined lateral and torsional loading conditions. For these tests, model response simulations were compared with experimental data only at global lateral load (overturning moment) vs. top displacement and torque vs. top twist rotation response levels, as detailed information on local deformation measurements was not available. Test results presented in the publications were digitized by the authors. During the tests, various base-overturning-moment-to-torque ratios were enforced on the wall specimens. During the analyses, the same overturning-moment-to-torque ratios were enforced on the wall models (proportional loading was applied using reference force vectors). In order to obtain the experimentally-measured top twist rotations of the walls, test measurements for the rotational displacements (i.e, relative lateral displacements) at the top of the walls were

post-processed. It must be noted that for load application purposes, each of these particular wall specimens incorporated a solid RC block at the top (Fig. 3), which would significantly restrain warping of wall cross-section under the applied torque.

It must be noted that the displacement-controlled loading procedures applied during testing and adopted in analysis of these wall specimens, were different from each other. During testing, neither the lateral displacement at the top of the walls (at the centroid of the wall cross-section), nor the top twist rotation of the walls was controlled. Instead, the lateral displacement at an ad-hoc point, which was located very close to the edge of the RC loading block at the top each wall, was controlled during each test. The top lateral displacement at the wall centroid and the top twist rotation of the wall were both measured. During analysis of each wall specimen, the top lateral displacement at the centroid of the wall cross-section was controlled (as measured during the test), and the corresponding top twist rotation of the wall was recorded, in order to better-investigate the influence of torsional demands on the analytical lateral load vs. displacement (i.e., flexural) response of the walls. Therefore, at instances of load reversal, the top twist rotations measured on the walls those predicted by the model may inherently differ.

Overturning moment vs. top lateral displacement and torque vs. top twist rotation response predictions of the LFSAFE model are compared in Fig. 21 with the experimentally-measured responses, for six representative H-shaped wall specimens subjected to different loading conditions. In specimen nomenclature, W corresponds to lateral loading in the weak direction of the wall cross-section (Fig. 2), S the strong direction, and D the diagonal (45-degree) direction. The number in specimen nomenclature indicates the percent ratio of the torque divided by the sum of the torque and overturning moment (maximum bending moment) values imposed on each specimen. When the measured and predicted overturning moment–top displacement responses of specimens HW25, HW50 and HW75 are compared (Fig. 21a, c, e), it can be observed that the overturning (bending) moment capacities of specimens HW50 and HW75 are both well-estimated (Fig. 21c, e). However, for specimen HW25 (Fig. 21a), since the model predicts degradation in load during the first loading cycle to positive 1.5% drift (whereas degradation in test results occurs during the second loading cycle to the same drift level) the model underestimates the bending moment capacity of this specimen by approximately 15% in the positive loading direction. Nevertheless, the model reasonably captures the lateral load degradation behavior and drift capacity of all three specimens, and well-simulates their hysteretic load–displacement response characteristics. Furthermore, and importantly, response comparisons presented for these specimens (Fig. 21a, c, e) clearly demonstrate that the LFSAFE model is capable of simulating the experimentally-observed reduction in wall bending moment capacity with increasing torque applied on the wall. For example, test results reported for wall specimens HW25, HW50, and HW75 reveal that the reduction in the bending moment capacity of the wall was measured as 3%, 53%, and 80% of that measured under pure shear/flexural loading (wall specimen HW00 Maruta et al. 1999), when torque-to-overturning-moment ratios of 0.33 (HW25), 1.0 (HW50), and 3.0 (HW75) were applied on the walls, respectively. The corresponding reductions predicted by the model are 6%, 46%, and 77%. However, these quantities cannot be generalized, as they are very dependent on the shear-span-to-depth ratio of the wall (as discussed by Hoult and Almeida 2024b, who analytically investigated the reduction in the bending moment capacity of U-shaped walls with increasing torque), as well as the wall cross-section and reinforcement, and the restraint imposed on the wall against warping.

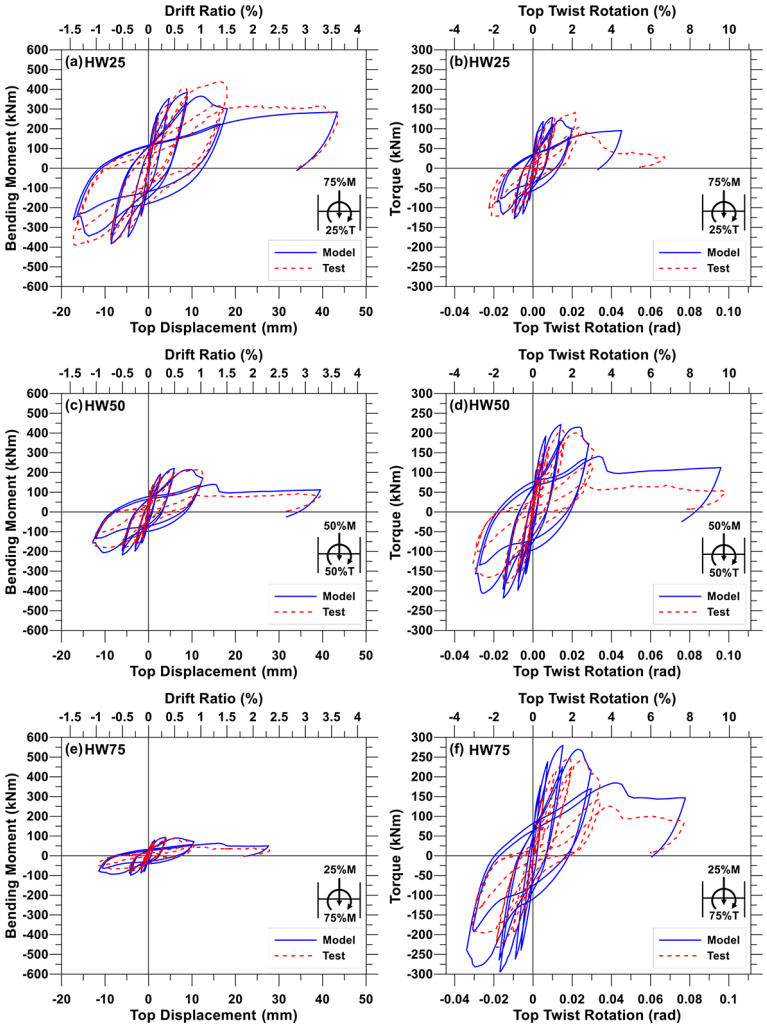

Fig. 21 Base overturning moment vs. top displacement and torque vs. top twist rotation responses for the H-shaped wall specimens

Comparison of model predictions with test measurements for the corresponding torque vs. top twist rotation response of these three specimens (HW25, HW50 and HW75) are presented in Fig. 21b, d, f. The model slightly underestimates the torque capacity of specimen HW25 in the positive loading direction, due to the aforementioned earlier strength loss prediction of the model. It should be noted that since the applied torques and overturning moments are proportional, degradation in bending moment and torque occur simultaneously in the test results and model predictions. The torque capacities of specimens HW50 and HW75 are moderately overestimated in the negative loading direction. The model successfully predicts the twist rotation values at the peaks (top displacement reversal points) of the loading cycles, except for specimen HW25, where the twist rotation at the positive peak of the last loading cycle is underestimated. Model estimations for the twist rotation capacity

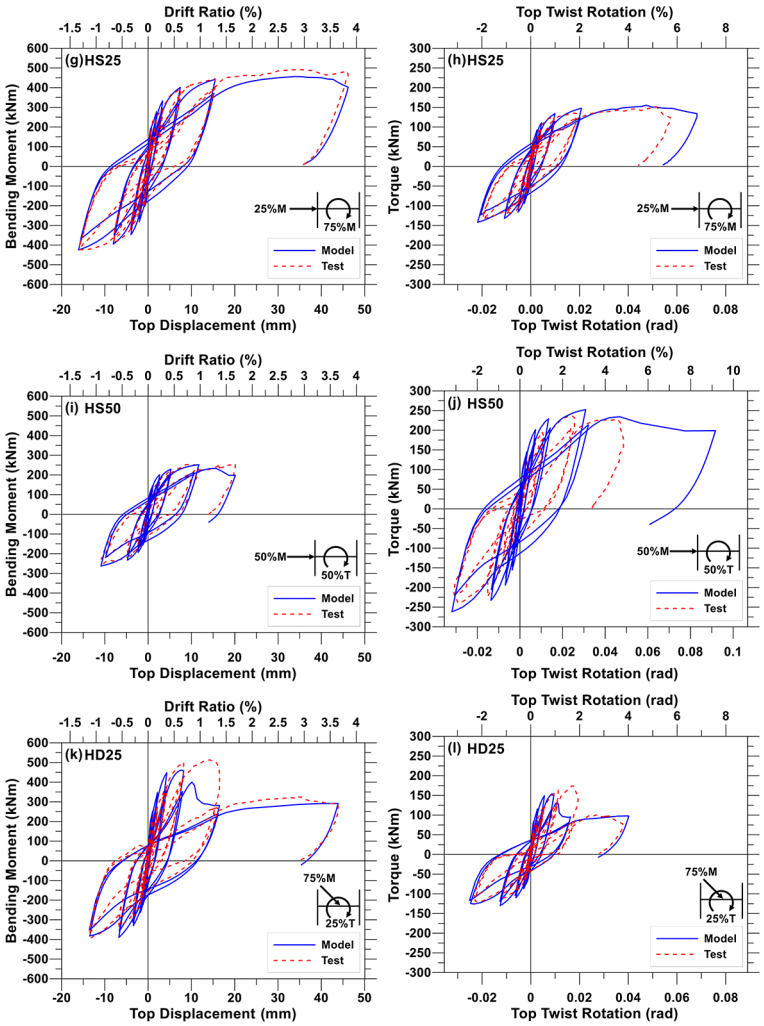

Figure 21 (continued)

of the walls (at initiation of torque degradation) are again, favorable. Hysteretic characteristics of the measured torque–twist rotation responses are generally well-simulated; however residual torque capacities after strength loss are somewhat overestimated. Results presented in Fig. 21b, d, f also highlight the reduction in wall torque capacity with increasing bending moment demand on the wall, demonstrating the capabilities of the LFSAFE model in simulating the experimentally-observed nonlinear torque-flexure interaction.

For wall specimens HS25 and HS50, for which the lateral loads were applied in the strong direction of the wall cross-section, the LFSAFE model provides more accurate predictions of the experimentally-measured overturning moment–top displacement and torque–top twist rotation responses. As shown in Fig. 21g, i. the model accurately simulates the bending moment capacities and hysteretic load–displacement response characteristics of both specimens, except for the slight yet sudden lateral load (bending moment) degradation

observed in the analysis results for specimen HS50 (Fig. 21i). Model predictions for the torque–twist rotation response of these walls are also favorable in terms of torque capacity and hysteretic behavior (Fig. 21 h, j), with the exception that the model significantly overestimates the twist rotation at the peak (top displacement reversal point) of the last loading cycle in positive rotation (Fig. 21j). This overestimation is associated with the slight yet sudden degradation that was observed only in the analytical bending moment–top displacement response of the wall (Fig. 21i), and is believed to be incidental.

Wall specimen HD25 was unique, in the sense that it is was the only specimen that was tested under bi-directional lateral loading combined with torsional loading. For this specimen, although the hysteretic response characteristics prior to strength loss are well-simulated similarly to specimen HW25, the model slightly underestimates the experimentally-measured bending moment and torque capacities in the positive loading direction (Fig. 21k, l), since model predicts an earlier degradation in load (which reflects to both bending moment and torque) compared to the measured response. Therefore, the model underpredicts the drift and twist rotation capacities of this specimen, although in the positive loading direction only. This discrepancy may also be incidental, because unlike other wall specimens, the experimentally-measured moment–displacement responses of this particular specimen are asymmetrical, in terms of measured moment and torque values measured in the two opposite loading directions. Furthermore, for all H-shaped wall specimens, the RC loading block located at the top of the walls is idealized in the analysis models using a fully-rigid constraint defined at the top of the wall models, which fully restrains warping of the wall cross-section at the top. Therefore, possible discrepancies between the analytically-assumed (rigid) and the actual stiffness characteristics of the loading block may have impaired the correlation between model results and test measurements. To the authors' knowledge, no information is available regarding possible cracking of the loading block during these tests. It must be noted that the fully-rigid loading block assumption was adopted in modeling in order to be able to analytically-apply the loading conditions (e.g., shear span) enforced on the wall specimens during testing. A sensitivity analysis on the influence of the assumed stiffness characteristics of the loading block on the model results could not be conducted, since currently-available linear elastic solid elements in OpenSees (for which the material elastic modulus can be calibrated) do not incorporate rotational DOFs at the element nodes, and cannot be used in combination with LFSAFE model elements.

Response comparisons presented in Fig. 21 also reveal that for most of the wall specimens, the experimentally-measured and analytically-predicted top twist rotations at the load reversal points of the response are in reasonable agreement, although this condition was not enforced in the analyses. As aforementioned, different displacement-controlled loading procedures were applied during testing and analysis of these walls. However, for specimens HW25 and HS50 (Fig. 21b, j) the measured and predicted top twist angles at the load reversal points were drastically different, although only during the final loading cycle in the positive torque direction, and after initiation of strength loss (degradation in lateral load and torque) in the overall wall response.

In terms of the experimentally-observed behavior and failure modes, all specimens were reported to exhibit flexural/torsional yielding of longitudinal reinforcement, and the reported failure mode (source of load degradation) of all specimens was crushing of concrete at wall flange boundaries under combined flexural and torsional (diagonal) compression, except specimens HS25 and HS50, for which concrete crushing was not reported. Analysis results

obtained for the walls also show yielding of longitudinal reinforcement, and degradation in load is associated with crushing of concrete and buckling of longitudinal reinforcement in flange boundary regions, which agrees with test observations. Overall, the response correlations presented demonstrate the effectiveness of the LFSAFE model in simulating the coupled nonlinear flexural and torsional responses of H-shaped walls subjected to combined lateral/torsional loading.

5 Future challenges

Development of an improved understanding of the coupled shear/flexural/torsional response characteristics of non-planar walls or complex wall systems (e.g., coupled core walls) under multi-directional dynamic excitations, is the foremost challenge. This requires not only further experimental studies on the subject, but also development of robust and extensively-validated modeling approaches/tools for RC walls. Such modeling tools need to be made available to the engineering community through widely-accessible computational platforms, facilitating their use in improved performance-based design/assessment methodologies to be adopted in real-life projects. The LFSAFE model element was developed and implemented in the open-source analysis platform OpenSees, as a step towards this objective.

Experimental validation studies presented in this paper clearly highlight the need for conducting further quasi-static tests on densely-instrumented non-planar wall specimens under combined lateral (both uni-directional and multi-directional) and torsional loading conditions. The boundary conditions imposed on the wall test specimens during testing must be as representative of real-life boundary conditions as possible (e.g., minimal warping restraint imposed on the wall specimen during testing). In cases where it is mandatory to integrate loading blocks/stubs/collars at the top of the wall specimens (e.g., in order to apply bending moment at the top of the wall for increasing its shear span), stiffness characteristics of these loading elements must be as quantifiable as possible, and possible damage to (e.g., cracking of) these elements during testing must be closely-observed and well-documented, since the warping restraint imposed by this element can influence the torsional response characteristics of the non-planar wall specimen.

A significant modeling challenge is related to simulating the experimentally-observed lateral instabilities at the flange boundaries (or along flanges) of non-planar walls, which are typically subjected to large tensile strain demands prior to crack closure upon load reversal. Such failures were commonly observed in RC wall buildings after the 2010 Chile and the 2011 Christchurch earthquakes. The inherent randomness associated with imperfect crack closure notwithstanding, even a multi-layered shell element is not mechanically capable of simulating out-of-plane instability, unless geometric nonlinearity is incorporated in its formulation. Although very detailed analytical studies have been conducted on this subject (e.g., recently by Dashti et al. 2017, 2018a, b, 2020), which focused mostly on planar walls, further studies that focus on modeling of lateral instabilities in non-planar walls under multi-directional lateral or combined lateral/torsional loading conditions, are still needed. Results of quasi-static tests conducted on non-planar wall specimens that exhibit lateral instability failures prior to concrete crushing (e.g., U-shaped wall specimens TUE and TUF tested by Hoult and Beyer 2021) would be very valuable in development and experimental validation of such modeling approaches.

6 Summary and conclusions

This paper presents a detailed and comprehensive study on simulating the hysteretic response characteristics of non-planar RC walls, using a new layered-shell model formulation. Response simulations conducted using the so-called Layered Fixed-Strut-Angle (LFSAFE) model, which is described in a companion paper (Tura et al. 2025), were compared in this paper with results of quasi-static tests conducted on heavily-instrumented non-planar wall specimens subjected to multi-directional loading conditions. Experimental calibration and validation of the model was conducted for U-shaped walls tested under uni-directional or bi-directional lateral loading, a U-shaped wall subjected to pure torsion, and H-shaped walls tested under combined lateral and torsional loading. Model response predictions were compared with test results at both global response (lateral load vs. top displacement, overturning moment vs. top displacement, torque vs. top twist rotation) and local deformation (e.g., flexural and shear deformation contributions to top displacement, vertical strain distribution across wall cross-section, vertical strain profile along wall height) levels. Based on the detailed response correlations presented in this paper, and bounded by the analysis results and experimental measurements considered in this study, the following conclusions are reached:

- The LFSAFE model is capable of simulating, with reasonable accuracy, the lateral load vs. top displacement response of U-shaped walls that are subjected to lateral loading and restrained against torsional twisting, irrespective of whether the lateral loading is uni-directional or multi-directional. The model is successful in predicting the lateral load capacity (in different loading directions), drift capacity, and lateral load degradation behavior of such walls, as well as their hysteretic load–displacement response characteristics, including unloading stiffness values, cyclic stiffness degradation, and pinching behavior. Experimentally-observed failure modes associated with crushing of concrete and buckling of longitudinal reinforcement in wall flange boundaries are reflected in the analysis results. However, the model cannot simulate failure modes related to out-of-plane buckling of wall flanges or rupture of reinforcing steel bars, since the present model element formulation does not incorporate geometric nonlinearity or reinforcement rupture.
- The LFSAFE model is shown to be also capable of providing accurate response predictions for a U-shaped wall subjected to pure torsion, in terms of its hysteretic torque vs. twist rotation response characteristics, as well as its torque capacity, twist rotation capacity, and torque degradation behavior. The model replicates the experimentally-observed concrete crushing in flange boundary of the torsionally-loaded U-shaped wall; however, the model is incapable of simulating the out-of-plane shear failure observed in the flange boundary, since its thin-shell formulation assumes linear-elastic through-thickness shear behavior.
- The LFSAFE model is also effective in simulating the coupled nonlinear flexural and torsional responses of H-shaped walls subjected to combined lateral and torsional loading. For various overturning-moment-to-torque ratios, the model consistently provides reasonable estimations of the experimentally-measured load–displacement and torque–twist responses of such walls, including strength degradation. For such walls, the model successfully simulates progressive reduction in wall flexural capacity with increasing

torque demand, as well as reduction in torque capacity of the wall under increasing bending moment demand. Concrete crushing in the flange boundaries of the H-shaped walls, under combined flexural and torsional compression demands, is reflected in the model response predictions.

- The LFSAFE model is shown to be successful in simulating the experimentally-observed nonlinear shear-flexure-interaction behavior in U-shaped walls, under both uni-directional and bi-directional lateral loading. In agreement with test measurements, the model predicts larger shear deformations in wall flanges subjected to flexural tension. As well, the model is capable of simulating migration of shear stresses towards regions subjected to larger axial compressive strains on a wall cross-section, and therefore provides a more reliable distribution of the internal shear forces developing in the web and flanges of non-planar walls under multi-directional lateral loading.
- For U-shaped walls subjected to bi-directional lateral loading or pure torsion, the LFSAFE model is shown to provide reasonable estimations of the magnitudes of longitudinal strains (both tensile and compressive) developing at different locations (flange tip, web-flange intersection, etc.) of the wall cross-section, as well as their distribution along wall height. Similarly to test measurements, longitudinal strain profiles predicted by the model along the wall cross section at the base of the wall are highly nonlinear (non-planar), under both lateral and torsional loading. Predicted and measured values for longitudinal strains are not always in agreement; however, a consistent discrepancy between strain predictions and measurements, which is common across the various tests, was not encountered. Consideration of strain penetration effects in analysis, albeit using an indirect and macroscopic modeling approach, improved the model predictions for the average longitudinal tensile strains at the base of the walls, without significantly influencing the global response estimations of the model. The layered (multiple-membrane) formulation of the model allows predicting the out-of-plane (through-thickness) strain gradient across the thickness of a wall segment, as was shown to agree with test measurements for a U-shaped wall under torsional loading. This strain gradient enables the LFSAFE model to provide better strain predictions on a wall cross sections (e.g., at the inner or outer wall surfaces or on multiple reinforcement layers), and allows simulating asymmetrical concrete crushing or asymmetrical reinforcement yielding across the thickness of a wall segment.

Overall, the LFSAFE model is shown to be a very effective and robust modeling approach for RC walls with non-planar geometries, as part of nonlinear static or dynamic analysis of three-dimensional wall systems or wall-frame systems, under multi-directional loads or excitations Dynamic response simulations conducted using the LFSAFE model are provided in the companion paper (Tura et al. 2025) presented in this special issue. The model is believed to be promising candidate for use in real-life performance-based design/assessment projects. The primary shortcoming of the model is failure to simulate out-of-plane instabilities (e.g., flange buckling) in walls, which is believed to be subject to improvement upon implementation of geometric nonlinearity in its formulation. The constitutive model for reinforcing steel will be improved to also represent post-buckling rupture. Further studies on experimental validation of the model will be conducted, particularly against shake table tests performed on isolated walls, wall systems, or wall-frame systems. Upon further

improvement/validation of the model and preparation of detailed user documentation, the model will be made publicly-available in OpenSees.

Acknowledgements The authors are grateful to Dr. Ryan Hoult and Prof. João Pacheco de Almeida from Université Catholique de Louvain, and Prof. Katrin Beyer from Ecole Polytechnique Fédérale de Lausanne, for sharing very valuable experimental data.

Author contributions All readers read and approved the final manuscript.

Funding Open access funding provided by the Scientific and Technological Research Council of Türkiye (TÜBİTAK).
The authors declare that no funds, grants, or other support were received during the preparation of this manuscript.

Data availability The datasets generated during and/or analyzed during the current study are available from the corresponding author upon reasonable request.

Declarations

Conflict of interest The authors have no relevant financial or non-financial interests to disclose.

Open Access This article is licensed under a Creative Commons Attribution 4.0 International License, which permits use, sharing, adaptation, distribution and reproduction in any medium or format, as long as you give appropriate credit to the original author(s) and the source, provide a link to the Creative Commons licence, and indicate if changes were made. The images or other third party material in this article are included in the article's Creative Commons licence, unless indicated otherwise in a credit line to the material. If material is not included in the article's Creative Commons licence and your intended use is not permitted by statutory regulation or exceeds the permitted use, you will need to obtain permission directly from the copyright holder. To view a copy of this licence, visit http://creativecommons.org/licenses/by/4.0/.

References

Abdullah SA, Wallace JW (2018) UCLA-RC walls database for reinforced concrete structural walls. Procs. of 11th National Conference in Earthquake Engineering, Los Angeles, California, USA

Ahmed KA, Lowes LN, Lehman DE (2023) Investigation of the behavior of slender reinforced concrete walls with complex configurations using nonlinear finite element analysis. Resilient Cities and Structures 2(1):120–142

American Society of Civil Engineers (2023) Seismic Evaluation and Retrofit of Existing Buildings. ASCE/SEI 41-23

Batoz JL, Tahar M (1982) Evaluation of a new quadrilateral thin plate bending element. Int J Numer Methods Eng 18(11):1655–1677

Behrouzi AA, Mock AW, Lehman DE, Lowes LN, Kuchma DA (2020) Impact of bi-directional loading on the seismic performance of C-shaped piers of core walls. Eng Struct 225:111289

Belarbi A, Hsu TTC (1994) Constitutive laws of concrete in tension and reinforcing bars stiffened by concrete. ACI Struct J 91:465–474

Beyer K, Dazio A, Priestley MJN (2008a) Quasi-static cyclic tests of two U-shaped reinforced concrete walls. J Earthquake Eng 12(7):1023–1053

Beyer K, Dazio A, Priestley MJN (2008b) Inelastic wide-column models for U-shaped reinforced concrete walls. J Earthquake Eng 12(S1)

Bilgin N (2018) Finite element modeling of nonrectangular reinforced concrete structural walls. M.S. Thesis, Bogazici University

Bilgin N, Gullu MF, Kolozvari K, Orakcal K (2021) Behavior and modeling of reinforced concrete walls, 9th Turkish Conference on Earthquake Engineering. Istanbul, Türkiye

Bruun EPG, Kuan A, Bentz EC (2020) How to model post-cracking torsional stiffness and why it matters. Int Concr Abstr Portal, ACI 344:49–63

Chang GA, Mander JB (1994) Seismic energy-based fatigue damage analysis of bridge columns: part 1-evaluation of seismic capacity. NCEER Technical Report No. NCEER-94-0006. Buffalo, USA
Coleman J, Spacone E (2001) Localization issues in force-based frame elements. ASCE J Struct Eng 127(11):1257–1265
Constantin R, Beyer K (2016) Behavior of U-shaped RC walls under quasi-static cyclic diagonal loading. Eng Struct 106:36–52
Dashti F, Dhakal RP, Pampanin S (2017) Numerical modeling of rectangular reinforced concrete structural walls. ASCE J Struct Eng 143(6)
Dashti F, Dhakal RP, Pampanin S (2018a) Blind prediction of in-plane and out-of-plane responses for a thin singly reinforced concrete flanged wall specimen. Bull Earthquake Eng 16:427–458
Dashti F, Dhakal RP, Pampanin S (2018b) Validation of a numerical model for prediction of out-of-plane instability in ductile structural walls under concentric in-plane cyclic loading. J Struct Eng 144:04018039
Dashti F, Dhakal RP, Pampanin S (2020) A parametric syudy on out-of-plane instability of doubly reinforced concrete structural walls. Part I: FEM predictions. Bull Earthquake Eng 18:3747–3780
Dassault Systemes (2016) SIMULIA-Abaqus/CAE user's guide
Dhakal RP, Maekawa K (2002) Modeling for post yield buckling of reinforcement. J Struct Eng 128:1139–1147
Feng DC, Ren XD, Li J (2018) Cyclic behavior modeling of reinforced concrete shear walls based on softened damage-plasticity model. Eng Struct 166:363–375
Filippou FC, Bertero VV PEP (1983) Effects of bond deterioration on hysteretic behavior of reinforced concrete joints. Report No. UCB/EERC-83/19, Earthquake Engineering Research Center, University of California, Berkeley
Gullu MF, Orakcal K (2021) Nonlinear finite element modeling of reinforced concrete walls with varying aspect ratios. J Earthquake Eng 25(10):2033–2064
Habasaki A, Kitada Y, Nishikawa T, Takiguci K, Torita H (2000) Multi-directional loading test for RC seismic shear walls. Procs. of 12th World Conference on Earthquake Engineering, Auckland, New Zealand
Hayami Y, Miyashita T, Maeda T (1991) Nonlinear analysis of shear walls, Procs. of 4th International Conference on Nonlinear Engineering Computations, Split, Yugoslavia
He XG, Kwan AKH (2001) Modeling dowel action of reinforcement bars for finite element analysis of concrete structures. Comput Struct 79:595–604
Hoult R (2019) Shear lag effects in reinforced concrete C-shaped walls. J Struct Eng 145(3):04018270
Hoult R, Bertholet A, Almeida JPd (2022) Vertical displacement and strain measurements of RC walls using fiber-optic sensors and conventional instrumentation. Procs. of 8th Asia conference on earthquake engineering, Taipei, Taiwan
Hoult R, Bertholet A, JPd A (2023c) Core versus surface sensors for reinforced concrete structures: a comparison of fiber-optic strain sensing to conventional instrumentation. Sensors 23(3):1745
Hoult R, Beyer K (2021) RC U-shaped walls subjected to in-plane, diagonal, and torsional loading: new experimental findings. Eng Struct 233:111873
Hoult R, Correia AA, JPd A (2023b) Beam-truss models to simulate the axial-flexural-torsional performance of RC U-shaped wall buildings. CivilEng 4(1):292–310
Hoult R, Doneux C, JPd A (2023a) Tests on reinforced concrete U-shaped walls subjected to torsion and flexure. Earthq Spectra 39(4):2685–2710
Hoult R, JPd A (2024a) Modified compression field theory and disturbed stress field model on the simulation of the global and local behavior of non-planar reinforced concrete walls under cyclic and dynamic loading. Bull Earthquake Eng. https://doi.org/10.1007/s10518-024-01982-1
Hoult R, JPd A (2024b) Flexure-torsion response of compressed open reinforced-concrete cores: experimental strain gradients, numerical methods, and interaction diagrams. J Struct Eng 150(9):04024111
Hoult R, JPd A, Correia AA (2024) Overview and blind prediction from shake table tests of a large-scale RC U-shaped core wall. Procs. of 18th World Conference on Earthquake Engineering, Milan, Italy
Ile N, Reynouard JM (2005) Behavior of U-shaped walls subjected to uniaxial and biaxial cyclic lateral loading. J Earthquake Eng 9(1):67–94
JPd A, Hoult R, Bertholet A, Candeias P, Carvalho A, Correia AA, Cumunel G, Doneux C, Han Y, Isakovic T, Janevski A, Lo Feudo S, Mihaylov B, Orgnoni A, Payen B, Palermo D, Pinho R, Ribeiro F, Simar A, Sousa ML (2024) Shake-table testing of two U-shaped RC walls: overview of the project ERIES-ALL4wALL. Procs. of 18th World Conference on Earthquake Engineering, Milan, Italy
Kajiwara K, Tosauchi Y, Sato E, Fukuyama K, Inoue T, Shiohara H, Kabeyasawa T, Nagae T, Fukuyama H, Kabeyasawa T, Mukai T (2017). 2015 Three-dimensional shaking table test of a 10-story reinforced concrete building on the E-defense part 1: overview and specimen design of the base slip and base fixed tests. Procs. of 16th World Conference on Earthquake Engineering, Santiago, Chile
Kitada Y, Nishikawa T, Takiguci K, Maekawa K (2007) Ultimate strength of reinforced concrete shear walls under multi-axes seismic loads. Nucl Eng Des 237(12-13)

Kolozvari K, Arteta C, Fischinger M, Gavridou S, Hube M, Isakovic T, Lowes L, Orakcal K, Vasquez J, Wallace JW (2018) Comparative study on state-of-the-art macroscopic models for planar reinforced concrete walls. ACI Struct J 115:1637–1657

Kolozvari K, Biscombe L, Dashti F, Dhakal RP, Gogus A, Gullu MF, Henry RS, Massone LM, Orakcal K, Rojas F, Shegay A, Wallace J (2019) State-of-the-art in nonlinear finite element modeling of isolated planar reinforced concrete walls. Eng Struct 194:46–65

Kolozvari K, Gullu MF, Orakcal K (2022) Finite element modeling of reinforced concrete walls under uni- and multi-directional loading using OpenSees. J Earthquake Eng 26(12):6524–6547

Kolozvari K, Kalbasi K, Orakcal K, Wallace J (2021a) Three-dimensional model for nonlinear analysis of slender flanged reinforced concrete walls. Eng Struct 236:112105

Kolozvari K, Kalbasi K, Orakcal K, Wallace J (2021b) Three-dimensional shear-flexure interaction model for analysis of non-planar reinforced concrete walls. J Build Eng 44:102946

LATBSDC (2023) An alternative procedure for seismic analysis and design of tall buildings, Los Angeles Tall Buildings Structural Design Council. Los Angeles, California

Li W, Li QN (2012) Seismic performance of L-shaped RC shear wall subjected to cyclic loading. Struct Des Tall Spec Build 21(12):855–866

Lu Y, Panagiotou M (2014) Three-dimensional cyclic beam-truss model for nonplanar reinforced concrete walls. J Struct Eng 140(3):04013071

Lu Y, Panagiotou M, Koutromanos I (2016) Three-dimensional beam-truss model for reinforced concrete walls and slabs–part 1: modeling approach, validation, and parametric study for individual reinforced concrete walls. Earthquake Eng Struct Dyn 45(9):1495–1513

Mander JB, Priestley MJN, Park R (1988) Theoretical stress-strain model for confined concrete. J Struct Eng 114:1804–1826

Mansour M, Hsu TTC, Lee JY (2002) Pinching effect in hysteretic loops of R/C shear elements. ACI Special Publication 205:293–322

Maruta M, Nishioka T, Suzuki N, Miyashita T (1999) H-shaped R/C core wall subjected to lateral load and torsion. J Struct Constr Eng, AIJ 524:103–110 (in Japanese)

Maruta M, Suzuki N, Miyashita T, Nishioka T (2000a) Structural capacities of H-shaped RC core wall subjected to lateral load and torsion. Procs. of 12th World Conference on Earthquake Engineering, Auckland, New Zealand

Maruta M, Suzuki N, Miyashita T, Nishioka T (2000b) Correlation between lateral load and torsion of H-shaped R/C core walls. J Struct Constr Eng, AIJ 532:153–160 (in Japanese)

Mazars J, Kotronis P, Ragueneau F, Casaux G (2006) Using multifiber beams to account for shear and torsion: applications to concrete structural elements. Comput Methods Appl Mech Eng 195(52):7264–7281

McKenna F, Fenves GL, Scott MH (2000) Open system for earthquake engineering simulation. University of California, Berkeley, California. http://opensees.berkeley.edu

Menegotto M, Pinto E (1973) Method of analysis for cyclically loaded reinforced concrete plane frames including changes in geometry and nonelastic behavior of elements under combined normal force and bending. Procs. of IABSE Symposium on Resistance and Ultimate Deformability of Structures Acted on by Well-defined Repeated Loads, Lisbon, Portugal

Ono H, Shintani K, Kitada Y, Maekawa K (2004) Restoring characteristics of shear wall subjected to horizontal two directional loading. Procs. of 13th World Conference on Earthquake Engineering, Vancouver BC, Canada

Orakcal K, Massone LM, Ulugtekin D (2019) A hysteretic constitutive model for reinforced concrete panel elements. Int J Concrete Struct Mater 13:1–23

Rojas F, Anderson JC, Massone LM (2019) A nonlinear quadrilateral thin flat layered shell element for the modeling of reinforced concrete wall structures. Bull Earthquake Eng 17:6491–6513

Saatcioglu M, Razvi SR (1992) Strength and ductility of confined concrete. J Struct Eng 118:1590–1607

Sato E, Tosauchi Y, Fukuyama K, Inoue T, Kajiwara K, Shiohara H, Kabeyasawa T, Nagae T, Fukuyama H, Kabeyasawa T, Mukai T (2017) 2015 Three-dimensional shaking table test of a 10-story reinforced concrete building on the E-defense part 2: specimen fabrication and construction, test procedure, and instrumentation program. Procs. of 16th World Conference on Earthquake Engineering, Santiago, Chile

Tassios TP, Vintzēleou EN (1987) Concrete-to-concrete friction. J Struct Eng 113:832–849

TBI-II (2017) Guidelines for Performance-Based Seismic Design of Tall Buildings - Version 2.03. Pacific Earthquake Engineering Research Center, Berkeley

Thermou GE, Papanikolaou VK, Kappos AJ (2014) Flexural behavior of reinforced concrete jacketed columns under reversed cyclic loading. Eng Struct 76:270–282

Tosauchi Y, Sato E, Fukuyama K, Inoue T, Kajiwara K, Shiohara H, Kabeyasawa T, Nagae T, Fukuyama H, Kabeyasawa T, Mukai T (2017) 2015 Three-dimensional Shaking Table Test of a 10-story Reinforced Concrete Building on the E-Defense Part 3: base Slip and Base Fixed Test Results. Procs. of 16th World Conference on Earthquake Engineering, Santiago, Chile

Tura C, Orakcal K, Gullu MF, Ilki A (2025) A new layered shell element for reinforced concrete walls I: model description and dynamic response simulations. Bull Earthquake Eng (accepted for publication)
Vassilopoulou I, Tassios TP (2003) Shear transfer capacity along a RC crack, under cyclic sliding. Proc. of FIB Symposium Concrete Structures in Seismic Regions (electronic source), Athens, Greece
Vecchio FJ, Collins MP (1993) Compression response of cracked reinforced concrete. J Struct Eng 119:3590–3610
Vintzēleou E, Tassios TP (1987) Behavior of dowels under cyclic deformations. ACI Struct J 84(1):18–30
Vintzēleou EN, Tassios TP (1986) Mathematical models for dowel action under monotonic and cyclic conditions. Mag Concr Res 38(134):13–22
Wang B, Wu MZ, Shi QX, Cai WZ (2023) Seismic performance of flanged RC walls under biaxial cyclic loading. J Build Eng 64:105632

Publisher's Note Springer Nature remains neutral with regard to jurisdictional claims in published maps and institutional affiliations.

Authors and Affiliations

Cem Tura[1] · Kutay Orakcal[1] · M. Fethi Gullu[2] · Alper Ilki[3]

✉ Kutay Orakcal
kutay.orakcal@bogazici.edu.tr

Cem Tura
cem.tura@bogazici.edu.tr

M. Fethi Gullu
fethigullu@harran.edu.tr

Alper Ilki
ailki@itu.edu.tr

[1] Bogazici University, Istanbul, Türkiye

[2] Harran University, Sanliurfa, Türkiye

[3] Istanbul Technical University, Istanbul, Türkiye